Meteoritics & Planetary Science 40, Nr 2, 261–295 (2005)
Abstract available online at http://meteoritics.org

Portales Valley: Petrology of a metallic-melt meteorite breccia

Alex RUZICKA[1*], Marvin KILLGORE[2], David W. MITTLEFEHLDT[3], and Marc D. FRIES[4]

[1]Cascadia Meteorite Laboratory, Portland State University, Department of Geology,
17 Cramer Hall 1721 Southwest Broadway, P.O. Box 751, Portland, Oregon 97207, USA
[2]Southwest Meteorite Laboratory, P.O. Box 95, Payson, Arizona 85547, USA
[3]NASA Johnson Space Center, Mail Code SN2, Houston, Texas 77058, USA
[4]Carnegie Institution of Washington, Geophysical Laboratory, 5251 Broad Branch Road Northwest, Washington, D. C. 20015, USA
[*]Corresponding author. E-mail: ruzickaa@pdx.edu

(Received 17 May 2004; revision accepted 30 December 2004)

Abstract–Portales Valley (PV) is an unusual metal-veined meteorite that has been classified as an H6 chondrite. It has been regarded either as an annealed impact melt breccia, as a primitive achondrite, or as a meteorite with affinities to silicated iron meteorites. We studied the petrology of PV using a variety of geochemical-mineralogical techniques. Our results suggest that PV is the first well-documented metallic-melt meteorite breccia. Mineral-chemical and other data suggest that the protolith to PV was an H chondrite. The composition of FeNi metal in PV is somewhat fractionated compared to H chondrites and varies between coarse vein and silicate-rich portions. It is best modeled as having formed by partial melting at temperatures of ~940–1150 °C, with incomplete separation of solid from liquid metal. Solid metal concentrated in the coarse vein areas and S-bearing liquid metal concentrated in the silicate-rich areas, possibly as a result of a surface energy effect. Both carbon and phosphorus must have been scavenged from large volumes and concentrated in metallic liquid. Graphite nodules formed by crystallization from this liquid, whereas phosphate formed by reaction between P-bearing metal and clinopyroxene components, depleting clinopyroxene throughout much of the meteorite and growing coarse phosphate at metal-silicate interfaces. Some phosphate probably crystallized from P-bearing liquids, but most probably formed by solid-state reaction at ~975–725 °C. Phosphate-forming and FeO-reduction reactions were widespread in PV and entailed a change in the mineralogy of the stony portion on a large scale. Portales Valley experienced protracted annealing from supersolidus to subsolidus temperatures, probably by cooling at depth within its parent body, but the main differences between PV and H chondrites arose because maximum temperatures were higher in PV. A combination of a relatively weak shock event and elevated pre-shock temperatures probably produced the vein-and-breccia texture, with endogenic heating being the main heat source for melting, and with stress waves from an impact event being an essential trigger for mobilizing metal. Portales Valley is best classified as an H7 metallic-melt breccia of shock stage S1. The meteorite is transitional between more primitive (chondritic) and evolved (achondrite, iron) meteorite types and offers clues as to how differentiation could have occurred in some asteroidal bodies.

INTRODUCTION

The Portales Valley (PV) meteorite is classified as an H6 chondrite (Grossman 1999), but it is atypical in that, unlike any other known ordinary chondrite, it contains coarse FeNi metal veins that exhibit Widmanstätten texture; it also exhibits a large variation in metal content in different specimens, ranging from metal-depleted to enriched (e.g., Kring et al. 1999a, 1999b; Rubin and Ulff-Møller 1999; Rubin et al. 2001; Ruzicka et al. 1999a, 1999b, 2000a; Pinault et al. 1999). Other unusual features include the presence of unusually coarse and abundant phosphate (Ruzicka et al. 1999a), large graphite nodules (Ruzicka et al. 2000b), and an unusually bright, red reflectance spectrum (Britt and Kring 2001). Another perplexing feature is that radiometric ages based on differing geochemical systems give discordant results (Chen et al. 1999, 2000; Papanastassiou et al. 2001, 2002; Garrison and Bogard 2001), which has led to differing interpretations (Papanastassiou et al. 2002; Floss et al. 2002; Ruzicka and Killgore 2002).

Mineral-chemical data, oxygen isotope data, and the presence of relict chondrules (e.g., Kring et al. 1999b; Rubin et al. 2001) support the general belief that Portales Valley originated as an H chondrite. However, the many anomalous features of PV suggest that it was processed in unusual ways. The role of shock in the origin of the meteorite is controversial. The shock stage of PV has been reported to be S1–S3 (Grossman 1999) and is listed in some data compilations as S3 (Koblitz 2003). This listing is based on the inference that the main features of the meteorite were established by shock and that subsequent annealing erased shock features (Kring et al. 1999b; Rubin and Ulff-Møller 1999; Rubin et al. 2001). Others have attributed only a minor role to shock (Pinault et al. 1999; Scott and Pinault 1999). An underlying point of agreement is that PV was partly melted, though the nature of this melting event has been debated. Possible origins include impact melting (Rubin et al. 2001), partial melting caused by endogenic heating (Pinault et al. 1999), collisions between differentiated and undifferentiated bodies (Ruzicka et al. 1999a, 2000a), or low-velocity collisions between accreting bodies that are already warm (Haack et al. 2000). Portales Valley has been alternately interpreted as an annealed impact melt breccia (Kring et al. 1999b; Rubin et al. 2001; Rubin 2004), a primitive achondrite (Pinault et al. 1999; Scott and Pinault 1999), or a meteorite transitional between chondrites and silicated iron meteorites (Ruzicka et al. 1999a, 2000a; Scott and Pinault 1999).

We studied Portales Valley using a variety of petrographic, mineralogic, chemical, and modelling techniques to better understand how it may have originated. Both geochemical and thermodynamic modelling were used to constrain the processes and conditions under which the meteorite formed. Our results indicate that PV is the first well-documented example of a metallic-melt breccia, and we suggest that it is transitional between chondrites and various classes of differentiated meteorites.

SAMPLES AND ANALYTICAL METHODS

A variety of analytical methods were used to study multiple samples of Portales Valley (Table 1). Eight polished sections of PV were studied using optical, scanning electron microscopy (SEM), electron microprobe (EMP), secondary ion mass spectrometry (SIMS), X-ray diffraction (XRD), and Raman techniques. These include five sections (4978-1–4978-5) of a specimen (AMNH 4978) that contains thin metal veins and large phosphate grains, a fine-grained silicate-rich sample (CML 0056-3) of a different specimen, and two slices (K-2, K-5) of a third stone containing coarse metal veins and a graphite nodule. The AMNH 4978 slices were removed from a specimen that formed a cube roughly 5 cm across, with four of the sections taken from adjacent locations on one face and the fifth from a perpendicular section (J. Boesenberg, personal communication 2000). The size of this specimen and the geometry of the cuts suggest that the sections sample a volume of ~125 cm^3 for the 4978 specimen.

Three electron microprobes were used to obtain quantitative phase data. A Cameca SX-50 was used to analyze olivine, orthopyroxene, phosphate, and FeNi metal at the University of Tennessee (UT) using an accelerating voltage of 15 kV and sample currents of 20 nA (silicate and phosphate) and 30 nA (metal). A different SX-50 was used to analyze FeNi metal and troilite at Oregon State University (OSU) using an accelerating voltage of 15 kV and a sample current of 50 nA. A Cameca SX-100 at the Johnson Spacecraft Center (JSC) was used to analyze olivine, orthopyroxene, clinopyroxene, FeNi metal, and troilite using an accelerating voltage of 20 kV and a sample current of 40 nA. Analyses of plagioclase were obtained at JSC using an accelerating voltage of 15 kV and a sample current of 20 nA. For all analyses except plagioclase, the beam was focussed to ~1 μm; for plagioclase, the beam was rastered over a 10 × 10 μm area. Counting times for each element varied from 20 to 120 sec depending on the phase being analyzed and the expected concentration of the element.

The UT microprobe was also used for electron petrography (BSE imaging) and X-ray modal mapping of all five AMNH sections. For modal mapping, X-ray energy dispersive spectra (EDS) were obtained from ~1 μm spots in a grid pattern with analysis spacings every 5.2 μm, using an Oxford Instruments (LINK) Model eXL II EDS and Feature Scan software. Operating conditions were a 20 kV accelerating voltage and a 3 nA sample current. Altogether, approximately 36 million EDS points were analyzed over an area of ~976 mm^2. Each EDS spectrum was classified into one of several phases based on X-ray line intensities (% peak area of regions of interest in the spectrum) for various elements. Once a spectrum was classified according to a particular phase, it was removed from consideration in the grid area. Test cases were run to obtain appropriate phase criteria and an appropriate phase identification sequence.

The sequence, elements, and X-ray peak intensities used to identify phases were: olivine (Si 30–50%, Mg 28–60%), orthopyroxene (Si 55–75%, Mg 18–27%, Ca 0–5%), kamacite (Fe 80–100%, Ni 0–6%), taenite (Ni 6.5–50%), troilite (S 30–100%), plagioclase (Al 10–40%, Si 55–85%), merrillite (P 25–75%, Cl 0–2%), apatite (P 25–70%, Cl 3–20%), clinopyroxene (Si 45–70%, Mg 5–18%, Ca 10–30%), chromite (Cr 15–70%), ilmenite (Ti 35–75%), Si-mineral (Si 85–100%), unclassified (none of the above). Roughly 9–16% of the points in the various sections remained unclassified; these included holes in the sections, epoxy from section edges, and grain boundaries. The precision of these modal data are difficult to quantify; we estimate precisions on the order of ~5% relative for each phase, in agreement with that of Gastineau-Lyons et al. (2002).

SIMS analyses were performed using a Cameca 3f at the Woods Hole Oceanographic Institution with the assistance of

Table 1. Samples used in this study.

Sample	Mass (mg)	Source[a]	Description
Samples of Portales Valley			
4978-1	–	AMNH	~1.7 cm wide, veined, polished thin section used for petrography and X-ray mapping
4978-2	–	AMNH	~1.7 cm wide, veined, polished thin section used for petrography, X-ray mapping, EMP and SIMS analyses
4978-3	–	AMNH	~1.7 cm wide, veined, polished section used for petrography and X-ray mapping
4978-4	–	AMNH	~1.7 cm wide, veined, polished section used for petrography and X-ray mapping
4978-5	–	AMNH	~2 cm wide, veined, polished section used for petrography, X-ray mapping, EMP and SIMS analyses
0056-3	–	CML	~4 × 2 cm wide polished thin section of silicate-rich portion used for petrography and EMP analyses
M-1	–	RH	Polished section of silicate fragments, used for EMP analyses
K-2	–	SML	~21 × 11 cm wide, veined, polished slab used for petrography and Raman analysis of graphite
K-5	–	SML	~16 × 13 cm wide, veined, polished slab used for petrography and XRD analysis of graphite
PVA	666	SML	Silicate-rich powder from aliquot A[b], analyzed at OSU with INAA
PVB	866	SML	Silicate-rich powder from aliquot A[b], analyzed at OSU with INAA
PVC	552	SML	Silicate-rich powder from aliquot B[c], analyzed at OSU with INAA
PVD	166	SML	Metal fragments (aliquot C[d]), analyzed at OSU with INAA
PVE	212	SML	Silicate-rich powder from aliquot A[b], analyzed at WSU with ICPMS
PVF	2017	SML	Silicate-rich powder from aliquot A[b], analyzed at WSU with XRF
PVG	293	SML	Silicate-rich powder from aliquot A[b], analyzed at PSU with INAA
PVH	73	RH	Silicate-rich powder of initially veined sample from aliquot D[e], analyzed at JSC with INAA
PVI	64	DB	Silicate-rich fragment from aliquot E[f], analyzed at JSC with INAA
Samples of El Hammami (H5) chondrite			
EH1	777	ET	Powder of unweathered material, analyzed at OSU with INAA
EH2	430	ET	Powder of unweathered material, analyzed at WSU with ICPMS

[a]Source code: AMNH = American Museum of Natural History; CML = Cascadia Meteorite Laboratory, section donated by Marvin Killgore; SML = Southwest Meteorite Laboratory, Marvin Killgore; ET = Edwin Thompson, sample donated by Timothy Gutschow and Dick Pugh; RH = Robert A. Haag via E. K. Gibson; DB = Don Bogard.

[b]Aliquot A = Three fragments and dust weighing a combined 5.719 g.

[c]Aliquot B = 1.72 g fragment observed to contain ~5 × 2 mm diameter grain of phosphate.

[d]Aliquot C = Two pieces visually estimated to contain 99% metal, obtained by cutting single 1.076 g coarse-metal-rich fragment.

[e]Aliquot D = 1.1 g sample that had been handpicked to remove coarser metal and fusion crust; observed to contain a yellowish opaque mineral, probably troilite.

[f]Aliquot E = portion of ~250 mg sample of coarsely crushed material that was prepared by D. D. Bogard for cosmogenic analyses.

Dr. Nobo Shimizu. In situ analyses for various rare earth elements (REE) and Ca were performed for phosphate minerals (merrillite, Cl-apatite) and low-Ca pyroxene (orthopyroxene) in different textural settings. Five cycles of counts were obtained in each analysis; count rates for each element were monitored between cycles to check for consistency and to evaluate whether overlap between phases could have occurred. Two standards (Durango apatite, KH-1 clinopyroxene) were analyzed in the same shift as the unknowns. Standard procedures were used to convert count rates for REE in the unknowns to concentrations, based on known REE and Ca abundances in the standards, and a Ca content in the unknowns obtained from EMP data. Uncertainties in concentrations were inferred from counting rate statistics.

X-ray diffraction and Raman analyses were obtained for a graphite nodule. XRD work was performed at the Applied Mineralogy Laboratory at Portland State University using Cu Kα radiation 2-theta angles stepped at 0.02° every 0.80 sec from 5° to 120° and an incident beam mask width of 5 mm with an irradiated length of 2 mm. Raman spectroscopy was performed using a Dilor XY modular laser Raman spectrometer at the University of Alabama with the Ar laser operating at a wavelength of 514.5 nm. The spectroscopy was performed as Stokes spectroscopy of an unpolished sample at room temperature with spectra collected through a 100× objective.

Nine additional samples, derived from five different bulk sample aliquots (A-E), were analyzed using instrumental neutron activation analysis (INAA), X-ray fluorescence (XRF), and inductively coupled mass spectrometry (ICPMS) techniques. These included pieces of silicate-rich fragments (PVA, PVB, PVC, PVE, PVF, PVG, PVH, PVI) and a nearly pure coarse-vein metal separate (PVD) (Table 1). Sample PVD was cut from a single coarse-vein fragment; the remaining samples were powders of silicate-rich material. Powders of PVA, PVB, PVC, PVE, and PVF were prepared by crushing fragments obtained from unweathered interior portions of the meteorite in a automated ceramic crusher, whereas a powder of PVH was produced by first using a stainless steel chisel to remove a fusion crust, then hand grinding with an agate mortar and pestle, and finally by removing lumps of coarser metal by handpicking. Sample PVH contained two small metal veins before crushing; sample PVC contained a phosphate patch approximately 5 × 2 mm across that was ground together with silicate. For

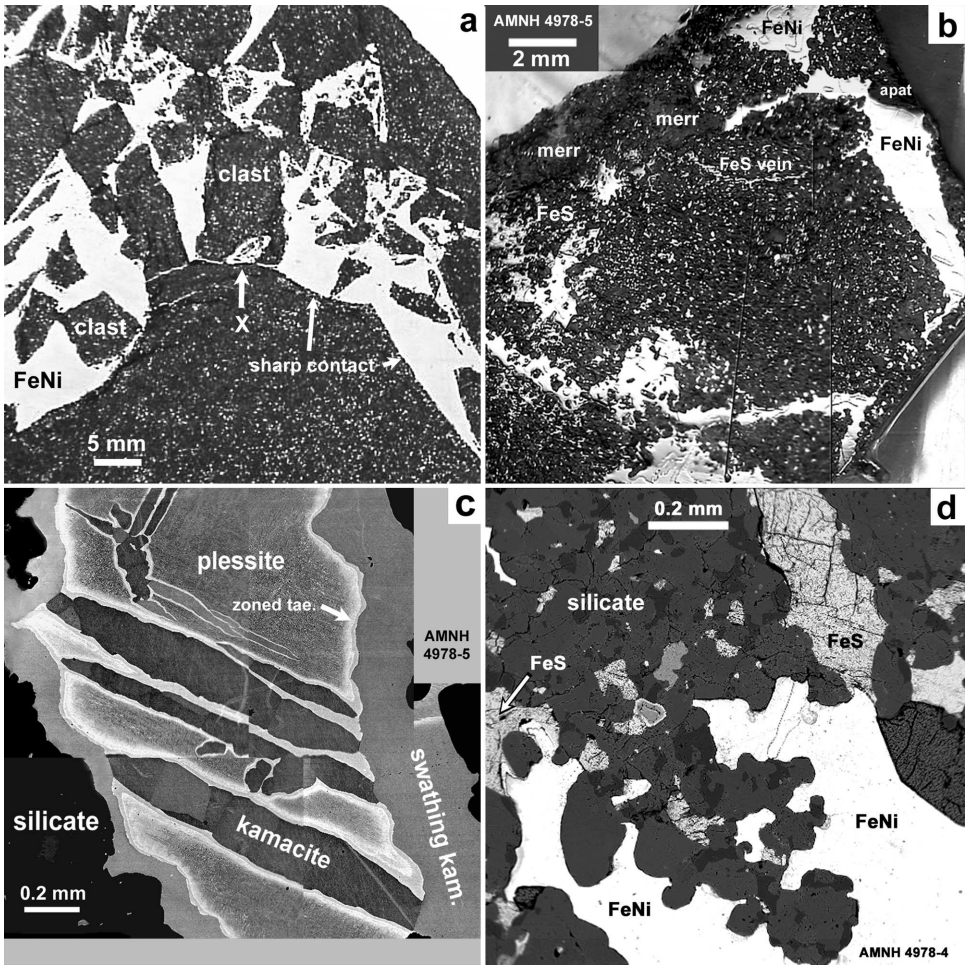

Fig. 1. Textural features of Portales Valley. a) Typical breccia or cataclastic texture seen with reflected light in polished slab (sample K-5), showing silicate-rich clasts enclosed by FeNi metal. Most clasts have sharp, straight boundaries; region X shows rounded metal-rich embayment inside a clast that appears to postdate clast formation. b) Sample AMNH 49788-5 seen in reflected light, consisting of veins of FeNi metal (FeNi) and troilite (FeS) that cross-cut silicate-rich areas. Coarse merrillite (merr) and Cl-apatite (apat) are found near the veins. Vein boundaries are irregular, and a clastic texture is not apparent. c) BSE image mosaic of metal vein in AMNH 4978-5 showing development of internal Widmanstätten texture and swathing kamacite at vein edges; with increasing distance from kamacite, metal is zoned from higher to lower Ni (white to grey, "zoned taenite") and finally to fine intergrowths of Ni-poor and Ni-rich metal (plessite). d) BSE image of FeNi metal vein (FeNi) that grades into troilite veins (FeS), with metal and troilite filling interstices of silicate grains (mainly low-Ca pyroxene); metal is convex outward against troilite (sample AMNH 4978-4).

comparison to Portales Valley, two bulk samples of the El Hammami Mountains (H5) chondrite were also analyzed using INAA and ICPMS techniques and the same procedures as employed for PV (Table 1). Analyses using INAA, ICPMS, and XRF were performed at multiple institutions. Samples PVH and PVI were analyzed at JSC using standard INAA procedures after being irradiated at the University of Missouri Reactor Facility for 12 hours with a neutron flux of 5.5×10^{13} neutrons $cm^{-2}s^{-1}$ (see Mittlefehldt and Lindstrom 1993 and references therein). These samples were analyzed along with some of the CM chondrites and Allende standard powders reported by Mittlefehldt (2002). Samples PVA, PVB, PVC, and PVD were analyzed at the OSU Radiation Center after 1 hr thermal (neutron flux 3×10^{12} $m^{-2}s^{-1}$) and 6 hr epithermal (neutron flux 1.2×10^{11} $cm^{-2}s^{-1}$) irradiations, and sample PVG was analyzed at Portland State University after irradiation at Reed Nuclear College Facility (neutron flux 1.7×10^{12} $cm^{-2}s^{-1}$). XRF analysis of sample PVF and ICPMS analysis of sample PVE were performed at the Washington State University (Pullman) Geoanalytical Lab. XRF analyses were obtained using a Rigaku 3370 XRF spectrometer using the procedures described by Johnson et al. (1999). ICPMS analyses were obtained using a Sciex Elan model 250 ICPMS using the procedures described by Knack et al. (1994). Uncertainties in INAA concentrations were estimated for each element based on the relative standard deviation in repeated counts of the element in the appropriate standard, or based on counting statistics of the element in the unknown, whichever was higher. Uncertainties in XRF data were estimated from the relative standard deviation in multiple

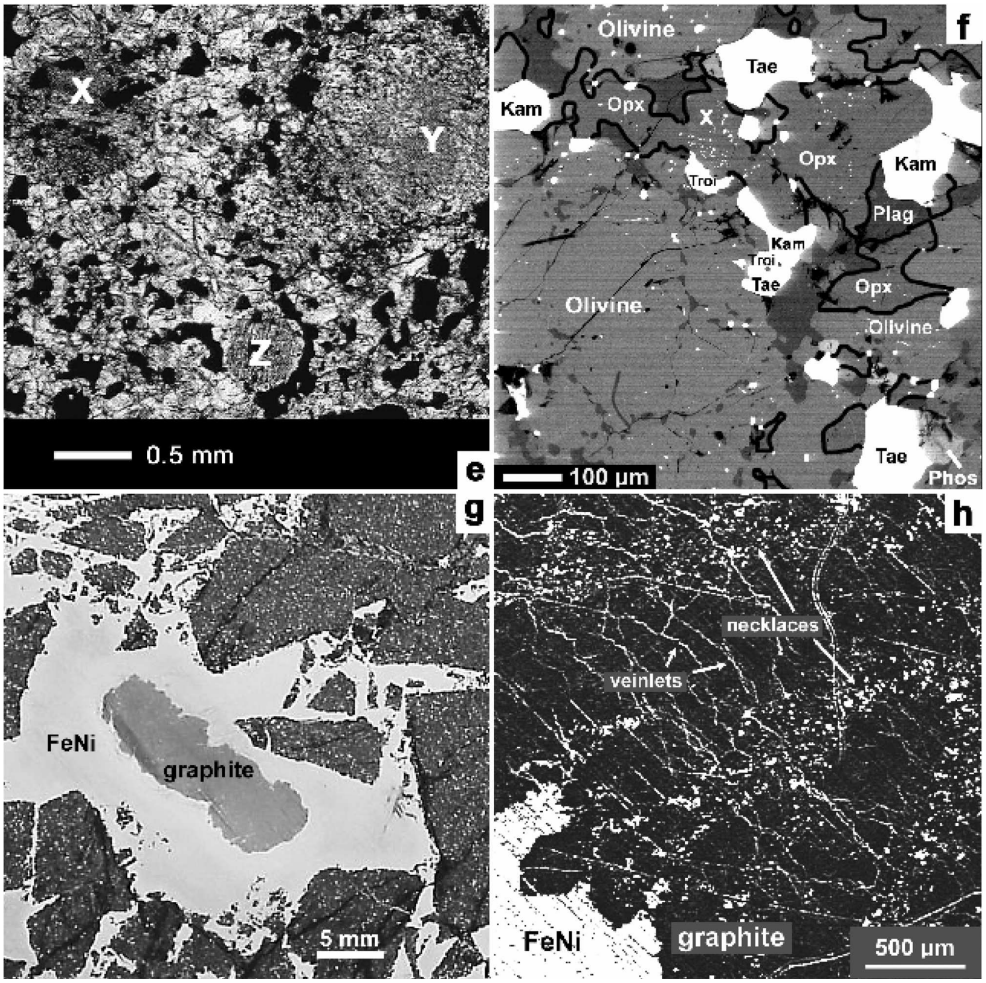

Fig. 1. *Continued*. Textural features of Portales Valley. e) Plane-polarized transmitted light view of silicate-rich sample (CML0056-3) showing three relict chondrules (X, Y, Z); black = opaque minerals (mainly metal and troilite); lighter areas = silicates. f) Silicate-rich sample (CML0056-3) observed in BSE showing anhedral grains of olivine, low-Ca pyroxene (Opx), plagioclase (Plag), kamacite (Kam), taenite (Tae), troilite (Troi) and phosphate (Phos); region X is an area of Opx that contains many fine-grained metal and troilite inclusions which could be locally "shock-blackened." g) Elongate graphite nodule enclosed in coarse Fe-Ni-metal (FeNi) (sample K-5, reflected light). h) Reflected-light view of graphite nodule in sample K-5 showing irregular nodule edge (bottom left) and two types of internal features, including irregular Fe-Ni-metal veinlets (trending upper left to lower right), and necklaces of FeNi metal inclusions (trending lower left to upper right); straight lines oriented from lower right to upper left are polishing scratches.

determinations for a standard (GSP-1) during a single XRF run over a three-week period. Uncertainties in ICPMS concentrations were estimated from the relative standard deviation in multiple determinations of two standards (BCR-P and TED) in different experiments between 1992–1994 (BCR-P) and 1995–1999 (TED).

RESULTS

Petrography and Mineralogy

Overall Petrography of Portales Valley

Although classified as an H6 chondrite, PV has various petrographic features atypical of chondrites. These include distinctive metal-veining textures, Widmanstätten texture in coarse FeNi metal veins, troilite veins, graphite nodules, and coarse phosphate (mainly merrillite, also Cl-apatite) that is usually in contact with metal. In contrast, silicate-rich areas have textures typical of a type 6 chondrite, although silicate grain sizes are fairly small (<100–200 µm), somewhat less than in other H6 chondrites (Rubin et al. 2001).

Metal-veining textures vary. Some areas show what appears to be cataclastic texture with silicate clasts of various sizes defined by metal veining (Fig. 1a); in other areas, metal veins appear intergrown with silicates and evidence for cataclasis is not obvious (Fig. 1b). Different sizes of metal veins are present, ranging from ~1–2 mm wide to >5 mm (even a few cm) wide. The coarsest metal veins appear to occur in areas with the best cataclastic texture (Fig. 1a), whereas thin metal veins are prevalent in more intergrown

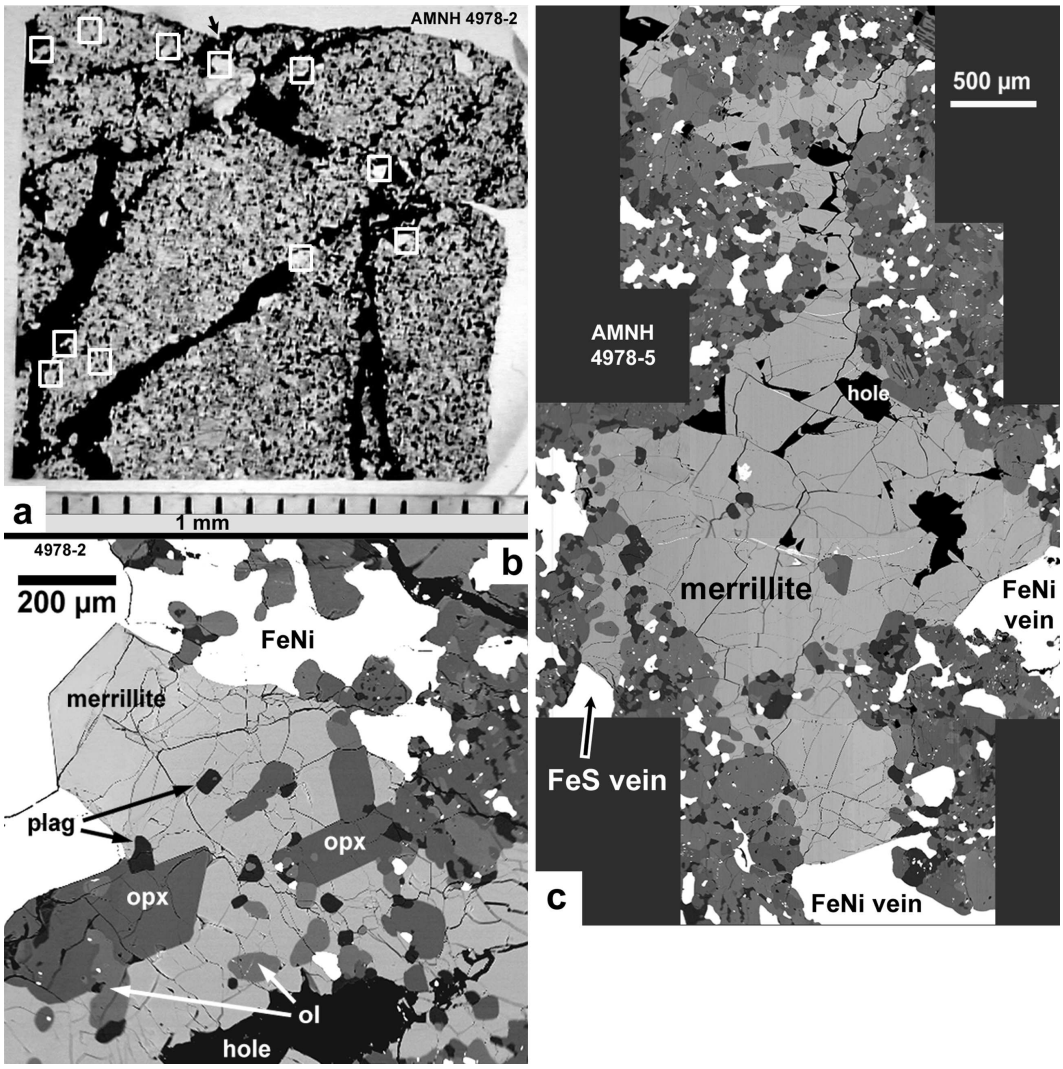

Fig. 2. Images illustrating the distribution and texture of phosphate grains in Portales Valley. a) Transmitted light view of AMNH 4978-2 showing preferred concentration of phosphate grains (located by white boxes) close to metal veins (black) that cross-cut silicate-rich areas. The scale at bottom has 1 mm increments. b) BSE image of the coarsest phosphate region in AMNH 4978-2 (indicated by arrow in Fig. 2a) showing merrillite which encloses euhedral-subhedral silicates (ol = olivine; opx = low-Ca pyroxene; plag = plagioclase) with an apparent poikilitic texture. c) BSE image of coarse vein-forming merrillite (light grey) extending from the termini of FeNi metal and troilite (FeS) veins (sample AMNH 4978-5).

areas (Fig. 1b). The textures of intergrown areas are suggestive of metamorphic grain growth, whereas the textures of cataclastic areas are more consistent with deformation. The sharp, relatively straight contacts between silicate and coarse metal veins in cataclastic areas (Fig. 1a) suggest relative movement of metal and silicate. In some areas, metal appears to have been injected into silicate clasts that were already formed, forming small metal-rich pockets (region "x" in Fig. 1a). This suggests that the metal was mobilized over an extended period of time.

Although most troilite in PV is intergrown with silicates away from metal veins, some veins of troilite are present that connect with and continue the trend of metal veins (Figs. 1b and 1d). At connection points with metal veins, troilite surrounds projections of metal and appears to have crystallized after metal (Fig. 1d). Troilite veins often appear to fill interstices between silicate grains, and metal veins in intergrown areas fill interstices between silicates (Fig. 1d). This texture implies crystallization of troilite and metal after silicates, with troilite apparently crystallizing last.

Widmanstätten texture (oriented kamacite lamellae enclosed within Ni-rich metal) occurs in metal veins that are ≥1 mm wide (Fig. 1c), with thinner veins showing an incipient Widmanstätten texture composed of isolated kamacite lamellae within Ni-rich metal. In areas with Widmanstätten texture, swathing kamacite separates silicate from the cores of veins that contain oriented kamacite lamellae surrounded successively by zoned taenite and

plessite (Fig. 1c). These features are absent in thinner veins, although like the coarser veins, kamacite often occurs at the contact with silicate, separating silicate from taenite in the core of the vein.

In silicate-rich areas, barely discernible relict chondrules are present (Fig. 1e). Grains in silicate-rich areas have predominantly anhedral shapes with an interlocking polymineralic texture (Fig. 1f), similar to that present in type 6 chondrites. Tiny metal and sulfide inclusions are present in some silicates (Fig. 1f). The textures we observed in our sections do not vary significantly, although Rubin et al. (2001) found that some silicate-rich areas in PV have many tiny metal and sulfide inclusions, which he interpreted as a shock-blackening effect (Rubin 1992). The overall texture of silicate-rich areas suggests that appreciable metamorphism of a chondritic precursor occurred but that melting, if any, was limited in extent.

Two centimeter-sized graphite nodules were found within coarse (2–4 cm across) metal areas. One of these nodules (Figs. 1g and 1h) was studied in detail after making multiple parallel cuts through it. Overall, the nodule has an irregular shape, varying from roughly equant to elongate, with an estimated volume of >2.3 cm^3. The contact between the nodule and enclosing metal vein is irregular in detail (Figs. 1g and 1h). Veinlets and inclusions of FeNi-alloy, largely or entirely kamacite, occur within the main graphite body (Fig. 1h). Most of the metal inclusions are <50 μm across, although they reach up to ~120 μm near the edges of the nodule. Kamacite veinlets in the nodule are of two types. One type consists of semi-continuous necklaces of metal inclusions that are often aligned perpendicular to the main axis of the nodule (Fig. 1h). The other type of vein consists of very thin, continuous veinlets (<2 μm wide) that have an irregular shape and which form a branching pattern (Fig. 1h). Based on the observations of inclusions of graphite inside metal and vice-versa, contemporaneous formation of metal and graphite is inferred.

Phosphate in PV is locally coarse (up to about a few mm wide), pale green, and occasionally forms veins. Phosphate is typically found adjacent to metal veins (Fig. 2a). The coarsest phosphate grains enclose silicate grains, including euhedral or subhedral grains of olivine, low-Ca pyroxene, and plagioclase in an apparently poikilitic texture (Fig. 2b). The same texture is observed in polymineralic veins dominated by merrillite. One vein is ~0.5–1 mm wide, ~6 mm long, and continues along the trend of both metal and troilite veins (Figs. 2c and 1b). The texture of coarse merrillite grains and veins could be interpreted to indicate that merrillite and the enclosed silicates crystallized from a melt (phosphate last), but it also could be interpreted as a poikiloblastic texture produced by metamorphism (phosphate overgrowing silicates).

Shock Stage and Deformation

We infer a low shock stage (S1) for PV based on traditional application of the Stöffler et al. (1991) petrographic shock scale. Olivine mainly has uniform extinction and generally lacks planar fractures or planar deformation features, although some planar features were reported present by Rubin et al. (2001). Our observations suggest that at most 5% of the olivine grains in PV have slight undulose extinction; the remainder show uniform extinction. Plagioclase has not been transformed to maskelynite and typically shows uniform extinction, although in most places it is too fine-grained to analyze reliably for extinction. No glassy melt pockets or pseudotachylite veins are present. An S1 shock stage for PV agrees with the listing given by Rubin (2004).

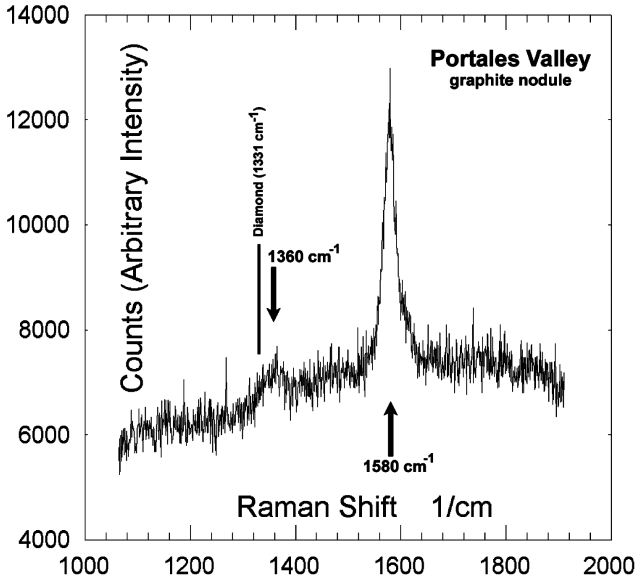

Fig. 3. Raman spectrum of graphite nodule in sample K-2 showing two peaks, a large peak at ~1580 cm^{-1} and a smaller peak at ~1360 cm^{-1}. No peak is apparent at the expected location for diamond at ~1331 cm^{-1}.

Although Portales Valley has a low shock stage, it shows evidence for deformation. The most obvious evidence for deformation is the cataclastic texture (see Overall Petrography of Portales Valley section). Silicate clasts have been displaced along metal veins, as observed in polished sections by previous researchers (Kring et al. 1999b; Rubin et al. 2001) and by us in handspecimen. In addition, approximately 5% of the larger olivine grains show undulose extinction, which is suggestive of shock deformation.

We obtained Raman spectra and X-ray diffraction (XRD) spectra for a graphite nodule that bear on the shock stage of PV. These techniques can detect diamond or other high-pressure polymorphs, and Raman spectra of graphite are useful shock barometers (Kenkman et al. 2002; El Goresy et al. 2002; Lapke et al. 2000). Verification of diamond or other high pressure polymorphs in the graphite would provide evidence that the graphite was shocked and possibly indicate an important role for shock in the origin of PV.

With XRD, we moved X-ray beams into different

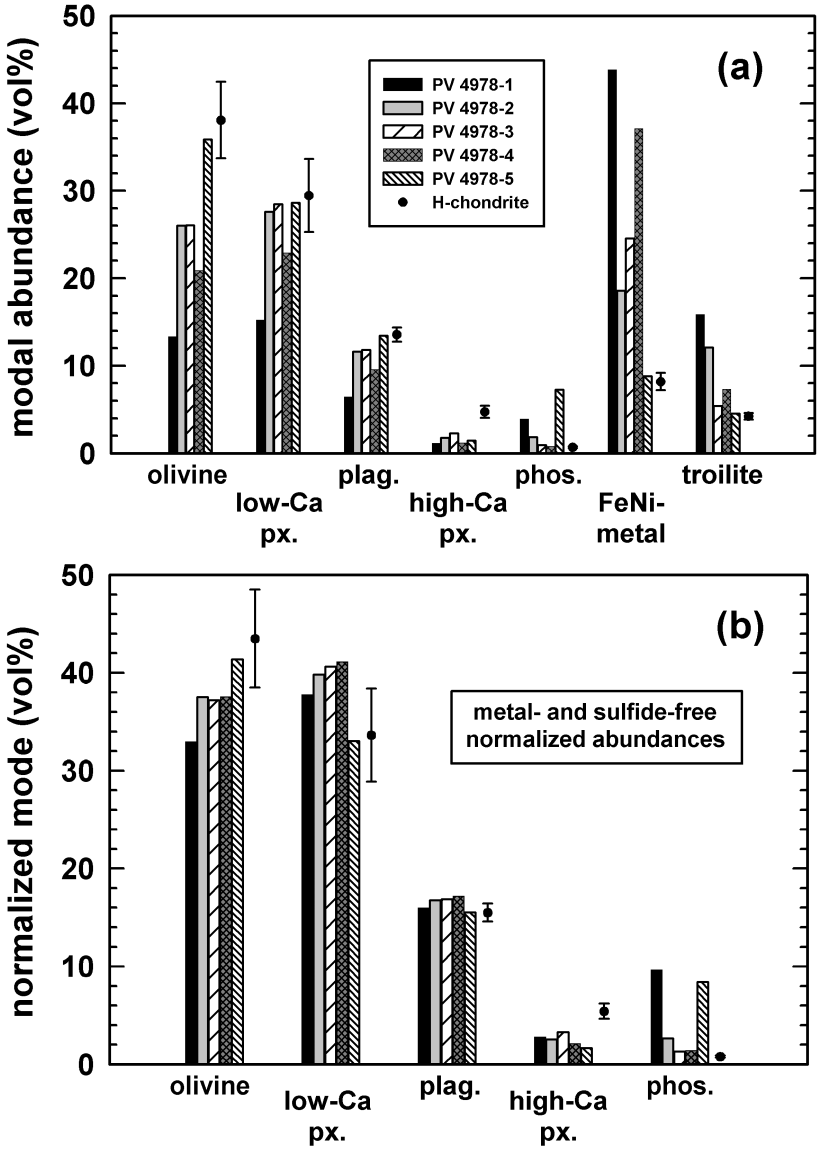

Fig. 4. Modal abundances in various sections of AMNH 4978. Data are compared to modes for H chondrites based on the data given in Jarosewich (1990); plotted H chondrite values show means (points) and standard deviations (bars). Compared to H chondrites, most samples of PV have low abundances of olivine and clinopyroxene (high-Ca px), and high abundances of low-Ca pyroxene (low-Ca px) and phosphate (phos).

locations in an attempt to locate diamond. Using a beam that illuminated only the vein enclosing the nodule, no graphite was detected and only kamacite and FeNi metal (a more Ni-rich metal) was detected. Using a beam that illuminated only the nodule, only graphite and kamacite was detected. No evidence for high-pressure polymorphs such as diamond, lonsdaleite, or chaoite was found.

Figure 3 shows the Raman spectrum for the nodule. The Raman spectrum shows peaks at ~1580 cm^{-1} and ~1360 cm^{-1} attributed to graphite and no peak at ~1331 cm^{-1}, as would be expected for diamond. Raman peaks at ~1318–1333 cm^{-1} for apparently shock-produced diamond inside graphite nodules from Canyon Diablo were found by Miyamoto (1998), but no such peaks are evident in the PV Raman spectrum (Fig. 3), consistent with the generally low shock stage for PV.

However, some disorder in PV graphite is implied by the Raman data. Crystalline graphite has a Raman "G-band" composed of merged peaks at ~1588 and 1582 cm^{-1}; with increasing disorder, a "D-band" occurs at ~1355 cm^{-1} (e.g., Kagi et al. 1991, 1994) and the 1582 cm^{-1} peak broadens and moves to lower frequencies (Kagi et al. 1994; Lapke et al. 2000). Disordered graphite with small domain size also produces a Raman peak at ~1620 cm^{-1}, which appears as a higher-frequency shoulder on the G-band (Kagi et al. 1994). The intensity ratio of the Raman G/D (1580/1360 cm^{-1}) peaks in graphitic carbon was attributed by Kagi et al. (1991) and

Table 2. Modal composition (vol%) of various sections of Portales Valley AMNH 4978 determined by X-ray mapping, compared to average H chondrite.

	4978-1[a]	4978-2[a]	4978-3[a]	4978-4[a]	4978-5[a]	4978 average	Avg. H chondrite[b]
vol%							
Olivine	13.3	26.0	26.1	20.9	35.9	24.4	38.09
Low-Ca pyroxene	15.2	27.6	28.5	22.9	28.6	24.6	29.47
High-Ca pyroxene	1.13	1.76	2.29	1.18	1.44	1.56	4.76
Plagioclase	6.45	11.6	11.8	9.56	13.5	10.6	13.59
Cl-apatite	3.10	0.15	0.17	0.02	5.10	1.71	–
Merrillite	0.80	1.69	0.75	0.77	2.17	1.24	–
Chromite	0.24	0.48	0.49	0.32	n.d.	0.31	0.57
Ilmenite	n.d.	n.d.	n.d.	n.d.	n.d.	0.00	0.18
Troilite	15.8	12.1	5.40	7.30	4.55	9.03	4.25
Low-Ni metal	25.6	14.1	13.5	23.8	6.75	16.7	–
High-Ni metal	18.2	4.50	11.1	13.3	2.05	9.83	–
Total FeNi metal	43.8	18.6	24.6	37.1	8.80	26.5	8.21
Total phosphate	3.90	1.84	0.92	0.79	7.27	2.95	0.71
Area mapped (mm^2)	~210	~215	~160	~176	~220		
No. of points ($\times 10^6$)	7.73	7.93	5.90	6.49	8.13		
Classified points (%)	83.9	89.4	89.0	91.0	91.3		

[a]Data normalized to 100% before rounding. n.d. = not detected.
[b]Normative composition (vol%) of average water-free, minimally weathered H chondrite (calculated from Jarosewich 1990).

Lapke et al. (2000) to the degree of structural ordering, ranging from amorphous (G/D ~1.3), to semi-ordered graphite (~2), to well-ordered graphite (~4), to "holo-ordered" graphite (∞) (Kagi et al. 1991). The G/D band intensity ratio for PV graphite is ~5.6, which implies that PV graphite is well-ordered but not holo-ordered. Additional evidence for minor disorder in PV graphite is provided by the G-band peak position (~1580 cm^{-1}) and high frequency shoulder (Fig. 3).

The XRD and Raman data for graphite allow a fairly precise estimate to be made of the shock pressure and shock stage of Portales Valley. Although disordering of PV graphite is relatively minor, shock pressures of just over approximately 5 GPa are implied, based on the calibration of the G/D Raman band intensity ratio provided by Lapke et al. (2000). Similarly, the failure to find diamond or other high-pressure C polymorphs in Portales Valley suggests shock pressures of less than 10–15 GPa, based on the calibration provided by Bischoff and Stöffler (1992). Thus, PV may have been shocked to pressures of about 5–10 GPa and, based on the Raman data, probably closer to about 5 GPa. This is somewhat above the S1-S2 transition pressure of about 4–5 GPa (Stöffler et al. 1991), but not by much.

Altogether, petrographic-mineralogic data suggest that a shock stage of S1, or at most S2, is appropriate for Portales Valley. The S3 shock stage listed in some data compilations (Koblitz 2003) is largely a model-dependent inference.

Modal Composition

Modal data for five sections of Portales Valley AMNH 4978 determined by X-ray modal mapping are given in Table 2. Data are shown normalized to 100% total in Fig. 4a and are normalized to metal- and sulfide-free abundances in Fig. 4b. Sample 4978 contains relatively small metal veins and is representative of an area containing neither very coarse (>1 cm wide) metal veins nor large silicate-rich regions depleted in metal, although it does contain coarse merrillite and apatite (Figs. 1b and 2). Based on X-ray mapping, the modal composition of PV significantly differs from that of H chondrites.

In various sections of sample 4978, metal and sulfide contents range from values typical to those found in H chondrites (in 4978-5) to three to four times enriched (in 4978-1) (Fig. 4a). Metal contents locally as high as ~45 vol% are observed; these are similar to those found in stony-iron meteorites. Phosphate abundances also vary dramatically, ranging from values similar to those in H chondrites (in 4978-4) to about ten times enriched (in 4978-5) (Fig. 4a, Table 2). The variations in phosphate and metal contents manifest the inhomogeneous distribution of these relatively coarse phases. Large variations in the abundance of metal also result in large variations in the abundances of other major phases such as olivine, orthopyroxene, and plagioclase. In contrast, the abundance of high-Ca pyroxene in PV is consistently depleted (by a factor of ~0.25×) compared to that typically present in H chondrites (Fig. 4a, Table 2). Clinopyroxene is relatively fine-grained in PV, and the consistently low abundance for it in the five sections examined implies that large portions of PV are depleted in this phase.

On a metal- and sulfide-free basis, the investigated sections of Portales Valley are significantly depleted in clinopyroxene, variably enriched in phosphate, and variably depleted in olivine and enriched in orthopyroxene (low olivine/pyroxene) compared to H chondrites (Fig. 4b). To first

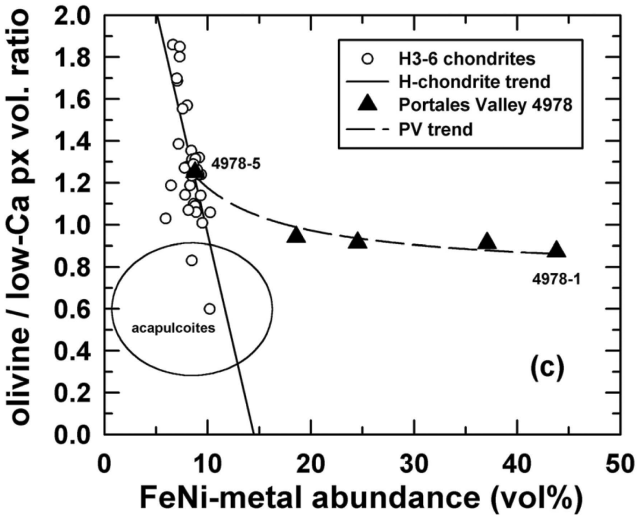

Fig. 5. Relationship between olivine/low-Ca pyroxene ratio and Fe-Ni metal abundance in various PV samples (AMNH 4978), compared to that in H chondrites (calculated from data given in Jarosewich 1990) and to the general field for acapulcoites (e.g., McCoy et al. 1996; Yugami et al. 1998). A first-order linear regression is shown for H chondrite data; a second-order regression is shown for PV data. In these PV samples, olivine/pyroxene ratios tend to be intermediate between H chondrites and acapulcoites, and metal contents tend to be higher.

approximation, the proportion of plagioclase in the non-metallic portion of PV is similar to that found in H chondrites, although some sections are slightly enriched in plagioclase (Fig. 4b).

The variable and generally low values of olivine/pyroxene in PV warrant comment. If such low values are real, they indicate that the silicate portion of PV as a whole cannot be considered to be an H chondrite. Figure 5 plots olivine/pyroxene abundance ratio and FeNi metal abundances for the five PV sections compared to H chondrites, with the latter based on normative calculations using bulk-chemical data (Jarosewich 1990). A field for acapulcoites, which are possible analogues to Portales Valley (Pinault et al. 1999; Scott and Pinault 1999), is also indicated. Figure 5 shows a crude correlation between olivine/pyroxene ratio and FeNi metal abundance in PV, with one section (4978-5) clearly having values typical for H chondrites and the other four sections having a low olivine/pyroxene ratio and high metal abundance. The apparent crude trend shown by PV differs from a correlation shown by H chondrites, which can be extended to the acapulcoite field (Fig. 5). An inverse relationship between olivine/pyroxene ratio and metal abundance is suggestive of a redox trend, but the one shown by PV clearly differs from the one seen within H chondrites or between H chondrites and acapulcoites.

Using the same X-ray mapping technique (with similar but not identical software and hardware parameters) and the same instrumentation as used here, Gastineau-Lyons et al. (2002) studied L and LL chondrites and found that modal olivine/pyroxene ratios inferred from mapping were systematically lower than what would be inferred from a normative calculation, for reasons that were unclear. If our data were subject to the same effect, apparently low olivine/pyroxene ratios might be an artifact of the procedures used. However, a systematic difference similar to that found by Gastineau-Lyons et al. (2002) cannot explain the H-like abundances of olivine, pyroxene, and FeNi metal in section 4978-5 (Figs. 4 and 5), unless this is pure coincidence. If our technique was underestimating olivine/pyroxene values, it should have done so consistently and not yielded an H-like ratio for the one section that also contains H-like metal abundances. Thus, we believe that the mapping technique we used provides accurate results and that the relatively low abundances of olivine and high abundances of orthopyroxene found in other sections of PV are not artifacts. Instead, the low olivine/pyroxene ratio seen in some sections of PV could be indicative of a redox effect.

Phase Compositions

Microprobe Data

Microprobe data for silicates and phosphate minerals are summarized in Table 3; microprobe data for FeNi metal and troilite are summarized in Table 4 and illustrated in Fig. 6. These data show that the major- and minor-element mineral chemistries of silicate, phosphate, and troilite in PV are generally similar to those in H chondrites, but that the composition of metal is somewhat unusual. In addition, with the exception of metal, the major phases in PV are chemically homogenous, suggesting a high degree of metamorphism.

Figure 6 shows Ni and Co contents in kamacite and taenite in PV compared to that in H and L chondrites. On this type of diagram, metal from H4-6 and L4-6 chondrites show similar but offset trends, with an overall negative correlation between Co and Ni contents caused by subsolidus equilibration to various closure temperatures, and the offsets between H and L chondrites caused by a difference in bulk composition and oxidation state between the two chondrite classes (Affiattalab and Wasson 1980; Brearley and Jones 1998). Cooling to lower closure temperatures results in higher Ni and lower Co contents in taenite and, ultimately, in lower Ni and slightly higher Co contents in kamacite. Thus, variations along inverse Ni-Co trends are the result of subsolidus processes, whereas differences in the position of the inverse trends reflect differences in bulk composition.

For PV kamacite and taenite, an overall inverse Ni-Co trend (Fig. 6) is seen consistent with what one would expect for subsolidus equilibration to various closure temperatures. This reflects intragranular zoning of metal, in which Ni contents are high and Co contents low on the margins of zoned taenite and Ni contents are slightly low on the margins of kamacite grains (Table 4). Moreover, Fig. 6 demonstrates that

Table 3. Mean composition of silicate and phosphate minerals in Portales Valley (sections 4978-2, 4978-5, M-1), determined by electron microprobe analysis. Numbers in parentheses refer to standard deviation of the mean; N = number of analyses averaged; n.a. = not analyzed.

	Olivine	Low-Ca pyroxene	High-Ca pyroxene	Plagioclase	Cl-apatite	Merrillite
wt%						
SiO_2	39.0 (0.15)	56.0 (0.3)	53.7 (0.4)	65.3 (0.2)	0.10 (0.03)	0.01 (0.01)
TiO_2	0.01 (0.01)	0.20 (0.03)	0.42 (0.09)	n.a.	n.a.	n.a.
Al_2O_3	0.01 (0.01)	0.22 (0.03)	0.57 (0.09)	21.8 (0.1)	n.a.	n.a.
Cr_2O_3	0.01 (0.01)	0.15 (0.03)	0.71 (0.19)	n.a.	n.a.	n.a.
FeO	18.3 (0.3)	11.5 (0.1)	4.26 (0.09)	0.39[a] (0.11)	0.15 (0.11)	0.38 (0.08)
MnO	0.46 (0.02)	0.48 (0.02)	0.21 (0.01)	n.a.	0.06 (0.03)	0.03 (0.02)
MgO	42.1 (0.6)	30.5 (0.3)	17.1 (0.2)	0.01 (0.01)	0.04 (0.01)	3.59 (0.05)
CaO	0.02 (0.2)	0.87 (0.20)	22.0 (0.4)	2.69 (0.06)	53.4 (0.3)	47.0 (0.2)
NiO	0.01 (0.0)	0.01 (0.02)	0.01 (0.00)	n.a.	n.a.	n.a.
Na_2O	<0.01	0.02 (0.01)	0.49 (0.08)	9.42 (0.13)	0.40 (0.05)	2.69 (0.05)
K_2O	n.a.	n.a.	n.a.	1.16 (0.16)	n.a.	n.a.
P_2O_5	n.a.	n.a.	n.a.	n.a.	40.8 (0.4)	46.0 (0.4)
Cl	n.a.	n.a.	n.a.	n.a.	5.66 (0.15)	0.01 (0.01)
Total	99.8	99.9	99.5	100.7	100.7	99.6
mol%[b]						
Fa	19.6 (0.5)	–	–	–	–	–
Wo	–	1.6 (0.4)	44.8 (0.4)	–	–	–
En	–	81.2 (0.3)	48.5 (0.3)	–	–	–
Fs	–	17.2 (0.2)	6.8 (0.2)	–	–	–
An	–	–	–	12.7 (0.3)	–	–
Ab	–	–	–	80.7 (0.9)	–	–
Or	–	–	–	6.6 (0.9)	–	–
N	39	41	13	28	13	18

Atomic formula units:
Olivine: $(Mg_{1.605}Fe_{0.391}Ca_{0.001}Mn_{0.010})Si_{0.996}O_4$
Low-Ca pyroxene: $(Mg_{1.612}Fe_{0.341}Ca_{0.033}Mn_{0.014}Na_{0.001}Cr_{0.004}Ti_{0.005})(Si_{1.984}Al_{0.009})O_6$
High-Ca pyroxene: $(Mg_{0.938}Fe_{0.131}Ca_{0.867}Mn_{0.007}Na_{0.035}Cr_{0.021}Ti_{0.012})(Si_{1.974}Al_{0.024})O_6$
Plagioclase: $(Na_{0.802}Ca_{0.127}K_{0.065}Fe_{0.014})(Al_{1.128}Si_{2.866})O_8$
Cl-apatite: $(Ca_{4.972}Fe_{0.011}Mg_{0.005}Mn_{0.004}Na_{0.068}Si_{0.009})(PO_4)_3Cl_{0.832}(OH,F)_{0.168}$
Merrillite: $(Ca_{2.586}Fe_{0.017}Mg_{0.276}Mn_{0.001}Na_{0.269})(PO_4)_2$

[a]Probable overestimate of true value, based on suspected secondary fluorescence from adjacent mafic phases.
[b]Fa = 100 Fe/(Fe + Mg); Wo = 100 Ca/(Ca + Mg + Fe); En = 100 Mg/(Ca + Mg + Fe); Fs = 100 Fe/(Ca + Mg + Fe); An = 100 Ca/(Ca + Na + K); Ab = 100 Na/(Ca + Na + K); Or = 100 K/(Ca + Na + K).

the Ni-Co trends in coarse vein metal and fine-grained metal in PV are offset from one another and from those in H and L chondrites. For taenite (>18 wt% Ni) with a given Ni content, Co is typically enriched in coarse vein taenite compared to fine-grained taenite (Fig. 6). In addition, although kamacite in coarse and fine-grained portions generally overlaps in Ni and Co contents, it differs at low (<5 wt%) Ni contents, with Co enriched in fine-grained metal (Fig. 6).

Differences in bulk composition probably partly account for the offset Ni-Co trends between fine and coarse metal in PV and in the offsets compared to metal in other H and L chondrites. Fine-grained metal in PV forms a trend with a generally similar slope to metal in H and L chondrites, but with a position intermediate between the two (Fig. 6). This implies that the fine-grained metal has bulk Ni and Co contents different from, and probably intermediate to, that of metal in H and L chondrites. The coarse vein metal in PV forms a more complex Ni-Co trend that is not parallel to that of H and L chondrites (Fig. 6). Coarse taenite with high Ni contents (>40 wt%) has Ni and Co contents that resemble those in fine-grained taenite, whereas coarse taenite with progressively lower Ni contents more closely resembles the metal found in L chondrites (Fig. 6). Our two independent estimates of the bulk composition of coarse vein metal (Table 4; see also Bulk Composition section) generally agree (Fig. 6), and these suggest that coarse vein metal in PV is somewhat enriched in Ni (~10–11 wt%) compared to bulk metal in H chondrites (~7–10 wt% [Chou et al. 1973; Rambaldi 1977; Kong et al. 1995]). Thus, Ni-Co data suggest that the coarse vein and fine-grained metal in PV have bulk compositions that differ from those in H and L chondrites and from each other.

The data also suggest that subsolidus closure temperatures in PV may have been somewhat lower for the fine-grained metal than for the coarse-grained metal. The evidence for this includes lower Ni contents in fine-grained

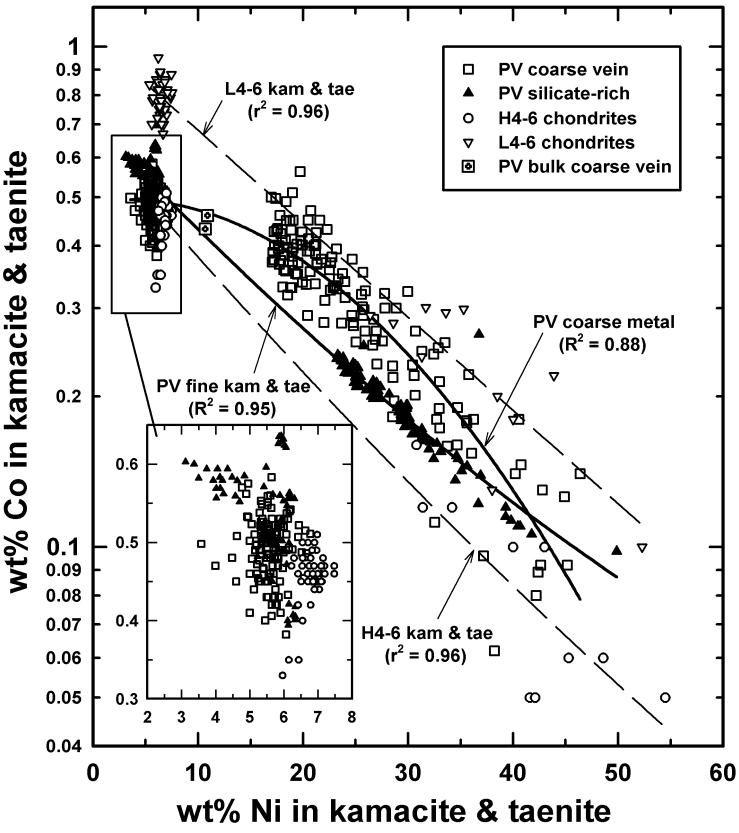

Fig. 6. Nickel and Co contents in individual analyses of kamacite (<7.5 wt% Ni) and taenite (>18 wt% Ni) in PV, compared to average compositions for kamacite and taenite in H4-6 and L4-6 chondrites (data from Rubin 1990; Affiatalab and Wasson 1980; Kong and Ebihara 1996; Kong et al. 1995). Second-order regressions are shown for fine-grained metal in PV (solid triangles), coarse vein metal in PV (open squares), H4-6 chondrites (open circles), and L4-6 chondrites (open triangles). Two estimates of bulk coarse vein in PV (Table 4, col. 8; Table 7, sample PVD) are also shown. See text for discussion.

kamacite than in coarse vein kamacite and higher average Ni contents in fine-grained taenite than in vein taenite (Fig. 6, Table 4). A relatively high closure temperature for the Ni-poor coarse taenite might also partly explain its anomalous ("L-chondrite-like") high Co content. These overall differences in closure temperature can be explained if intragranular Ni-Co diffusion in metal was much slower than grain boundary diffusion.

SIMS Data

Trace element SIMS data were obtained for eight rare earth elements (REE) in low-Ca pyroxene and in phosphate minerals in two sections of Portales Valley. These data are shown in Table 5 and Fig. 7. Low-Ca pyroxene (orthopyroxene) analyses were obtained for grains in different settings, including grains poikilitically enclosed within phosphate, a grain enclosed by metal, and a typical orthopyroxene grain in a silicate-rich area. Analyses were also obtained for both coarse Cl-apatite and merrillite associated with metal veins and for a typical fine-grained merrillite in a silicate-rich area.

CI-normalized REE abundances in all of the orthopyroxene grains are flat to slightly depleted in light REE (LREE) (Fig. 7a). There is no obvious difference between grains in different textural settings. Anomalously high Ce abundances were obtained for one of the orthopyroxenes (analysis 2-1-3) enclosed within phosphate (Fig. 7a). For this analysis, counts for Ce dropped after the first of five cycles, suggesting that the high Ce content is an artifact of weathering. For the orthopyroxene analyzed in a silicate-rich area (analysis 2-6-2), Eu counts increased significantly in the last three cycles, suggesting that the SIMS beam penetrated to a Eu-rich phase (plagioclase). Altogether, the overall REE abundances in low-Ca pyroxene appear to be somewhat low in PV compared to other equilibrated ordinary chondrites (EOCs) (Fig. 7a). This could indicate that some of the REE normally found in orthopyroxene was partitioned into an REE sink such as phosphate or clinopyroxene.

In general, REE abundances of Cl-apatite and merrillite resemble those in ordinary chondrites (Fig. 7b). Cl-apatite has a CI-normalized LREE-enriched pattern with a positive Eu anomaly (Fig. 7b). REE concentrations in merrillite vary

Table 4. Mean composition of FeNi metal and troilite in Portales Valley, determined by electron microprobe analysis. Numbers in parentheses refer to the standard deviation of the mean; N = number of analyses; n.a. = not analyzed.

	Silicate-rich areas (1–3)			Coarse veins with Widmanstätten texture (4–8)				
	Kamacite 1	Taenite 2	Troilite 3	Kamacite 4	Kamacite margins 5	Zoned taenite 6	Plessite 7	Bulk 8
wt%								
Fe	93.5 (0.8)	71.1 (4.6)	64.0 (0.1)	93.0 (0.6)	93.9 (0.6)	73.4 (7.8)	84.2 (5.4)	87.7 (6.9)
Co	0.55 (0.07)	0.19 (0.03)	<0.01	0.49 (0.04)	0.50 (0.05)	0.32 (0.10)	0.44 (0.07)	0.46 (0.08)
Ni	5.29 (0.94)	28.9 (4.8)	0.01 (0.01)	5.72 (0.38)	5.08 (0.24)	25.0 (7.3)	14.8 (5.4)	10.9 (6.9)
P	0.01 (0.01)	0.01 (0.01)	<0.01	0.01 (0.01)	0.01 (0.01)	0.01 (0.01)	0.01 (0.01)	0.01 (0.01)
Cr	0.01 (0.01)	<0.01	0.01 (0.01)	<0.01	<0.01	<0.01	<0.01	<0.01
S	0.02 (0.01)	0.02 (0.02)	36.8 (0.1)	n.a.	n.a.	n.a.	n.a.	n.a.
Total	99.4	100.2	100.9	99.2	99.4	98.7	99.5	99.1
wt.								
Co/Ni	0.10	0.0066	–	0.086	0.098	0.013	0.030	0.042
N	55	91	6	109	11	141	193	50

1, 2: Grains of "fine-grained" metal alloy, including kamacite (3.1–6.3 wt% Ni) and taenite (23.2–49.9 wt% Ni), analyzed in section 0056-3 and section M-1.
3: Grains analyzed in section M-1.
4: Kamacite lamellae and swathing kamacite (5.0-6.9 wt% Ni) in coarse-grained alloy from section 4978-5.
5: Margins of kamacite grains (lamellae and swathing kamacite) in coarse-grained alloy (4.6–5.3 wt% Ni) adjacent to zoned taenite in section 4978-5.
6: Zoned FeNi metal alloy (17.0-46.4 wt% Ni) adjacent to kamacite lamellae in section 4978-5.
7: Average composition of plessite (decomposed martensite) in coarse alloy (apparent Ni content = 4.2–34.5 wt%) within largest vein in section 4978-5.
8: Estimated composition of largest vein in section 4978-5, based on analyses obtained in a traverse down the vein axis.

considerably, although all have similar CI-normalized abundance patterns with a prominent negative Eu anomaly, a generally flat to heavy REE (HREE) depleted pattern, and the highest CI-normalized abundances occurring for Nd (Fig. 7b). Again, there is no obvious difference between coarse phosphate associated with metal veins and with fine-grained phosphate in silicate-rich areas.

Bulk Composition

Different splits of Portales Valley were analyzed for bulk major and trace element abundances using INAA, XRF, ICPMS, and modal reconstruction (Table 1). Sample PVD is a fragment of coarse vein metal; samples PVA, PVB, PVC, PVE, PVF, PVG, PVH, and PVI are samples of metal-poor, silicate-rich material; different sections of sample 4978 have small metal veins and an overall intermediate metal content. A reference H5 chondrite, El Hammami Mountains, was analyzed for comparison. Chemical data are given in Tables 6–8.

Figure 8 shows major element data normalized to Si and H chondrites (Jarosewich 1990) for metal-poor sample PVF and for the metal-veined sections of 4978. Compared to H chondrites, the metal-poor sample is highly depleted not only in metal (Fe/Si, Ni/Si), but also in phosphate (P/Si, Ca/Si), and otherwise resembles an H chondrite. The metal-veined samples are mostly enriched in metal (Fe/Si, Ni/Si) and troilite (S/Si), show slight excesses in feldspar (Na/Si, K/Si, Al/Si), and are consistently low in ilmenite (Ti/Si) and enriched in phosphate (P/Si). Ca/Si values in the 4978 samples are not always superchondritic despite elevated phosphate (P/Si) abundances (Fig. 8), because clinopyroxene is depleted (see Modal Composition section).

As with the major elements, trace element data for silicate-rich samples document spatial variations in composition, primarily of those elements that concentrate in phosphate and in metal. This undoubtedly reflects an inhomogeneous distribution of these phases. Siderophile element abundances are generally depleted in these samples compared to El Hammami, as one might expect for metal-poor samples, but abundance patterns are fractionated (Fig. 9a). With regard to lithophile elements, different silicate-rich samples vary in their abundances of those elements (REE, Y, and to a lesser extent Th) that normally concentrate in phosphate. Sample PVC is enriched in these elements and samples such as PVE are depleted in them (Figs. 9a and 9b). The lack of significant variation in other incompatible trace elements such as Zr, Nb, Hf, Rb, and Sr as well as the uniform abundances of the semi-incompatible Sc (Figs. 9a and 9b) make it clear that significant chemical variations in PV are not caused by standard igneous processes, but by an inhomogeneous distribution of phosphate.

Trace element and Ni abundances of the coarse metal separate from PV (PVD) (Table 7) are grossly similar to that of average metal in H4-6 chondrites (Chou et al. 1973; Rambaldi 1977; Kong et al. 1995), but are different in detail. In both PVD and two samples of coarse metal analyzed by Rubin et al. (2001), Ga and Au abundances are higher than in H chondrites. Nickel abundances in both our sample of coarse metal and the one analyzed by Rubin et al. (2001) are significantly higher than in H chondrite metal. We also found

Table 5a. Trace element composition of phosphate in Portales Valley (4978-2, 4978-5), determined by SIMS analysis. Values are given in μg/g; those in parentheses refer to the estimated precision, based on counting statistics.

Analysis[a]	La	Ce	Nd	Sm	Eu	Dy	Er	Yb	Comment
Cl-apatite									
5-5-1	8.81 (0.09)	21.3 (0.2)	12.3 (0.1)	2.81 (0.05)	1.37 (0.03)	3.55 (0.07)	2.11 (0.05)	1.99 (0.05)	coarse; pair 5-5A
Merrillite									
5-5A-1	42.6 (0.2)	129.4 (0.4)	111.2 (0.4)	34.3 (0.2)	1.91 (0.04)	45.5 (0.3)	26.7 (0.2)	24.4 (0.2)	coarse; pair 5-5
5-3-1	45.7 (0.2)	134.3 (0.4)	103.2 (0.4)	30.1 (0.2)	2.42 (0.05)	36.0 (0.2)	21.1 (0.2)	22.0 (0.2)	coarse
5-1-1	50.0 (0.2)	148.8 (0.4)	127.9 (0.4)	41.5 (0.2)	2.40 (0.04)	59.5 (0.3)	34.2 (0.2)	29.4 (0.2)	coarse vein
2-1-1	55.5 (0.3)	167.6 (0.6)	141.7 (0.5)	45.0 (0.3)	2.57 (0.06)	67.1 (0.4)	40.8 (0.3)	31.4 (0.3)	coarse
2-1-2	56.2 (0.3)	166.2 (0.5)	139.2 (0.5)	43.8 (0.2)	2.40 (0.05)	66.9 (0.3)	39.7 (0.3)	31.2 (0.2)	coarse
2-6-1	54.1 (0.3)	153.7 (0.6)	123.4 (0.5)	35.5 (0.3)	1.92 (0.05)	51.9 (0.3)	31.6 (0.3)	24.8 (0.2)	matrix, finer
Mean merr.	50.7	150.0	124.4	38.4	2.27	54.5	32.3	27.2	

[a]Nomenclature for analyses in Tables 7a and 7b as follows: first digit indicates section number (2 = AMNH 4978-2, 5 = AMNH 4978-5), second digit indicates analysis region in section, and third digit indicates analysis number in region.

Table 5b. Trace element composition of orthopyroxene in Portales Valley (4978-2), determined by SIMS analysis. Values are given in ng/g; those in parentheses refer to the estimated precision, based on counting statistics.

Analysis[a]	La	Ce	Nd	Sm	Eu	Dy	Er	Yb	Comment
2-6-2	14.4 (2.3)	27.1 (4.0)	28.8 (3.7)	40.0 (4.3)	106 (6)	16.0 (2.8)	33.5 (3.7)	27.4 (3.9)	all 5 cycles
2-6-2	15.9 (4.2)	27.2 (6.2)	20.1 (4.8)	27.7 (5.2)	9.3 (3.0)	19.7 (4.4)	31.0 (5.6)	24.1 (5.1)	first 2 cycles
2-1-3	116 (7)	795 (20)	44.4 (4.5)	42.3 (4.3)	3.9 (1.1)	26.7 (3.2)	33.8 (3.6)	69.8 (5.5)	all 5 cycles
2-1-3	107 (8)	592 (21)	42.6 (4.9)	43.1 (4.5)	5.1 (1.6)	27.3 (3.6)	31.5 (4.0)	74.5 (6.4)	last 4 cycles
2-1-4	10.7 (2.2)	6.4 (1.9)	21.6 (3.1)	41.8 (4.2)	5.6 (1.4)	17.0 (2.4)	29.4 (3.5)	70.0 (6.3)	
2-1-5	24.5 (4.1)	86.3 (8.9)	20.6 (2.9)	36.2 (5.0)	3.6 (1.2)	57.7 (6.4)	43.2 (5.1)	79.9 (7.9)	
2-1-6	0.6 (0.2)	9.9 (2.6)	23.5 (3.4)	33.6 (4.0)	12.2 (2.7)	23.6 (3.9)	40.5 (4.6)	54.3 (5.3)	
Mean[b]	12.9	32.4	26.0	36.3	6.9	29.0	35.6	59.6	

[a]Nomenclature for analyses in Tables 7a and 7b as follows: first digit indicates section number (2 = AMNH 4978-2, 5 = AMNH 4978-5), second digit indicates analysis region in section, and third digit indicates analysis number in region.

[b]Uses first two cycles of 2-6-2 and last four cycles of 2-1-3; excludes high La and Ce values of analysis 2-1-3.

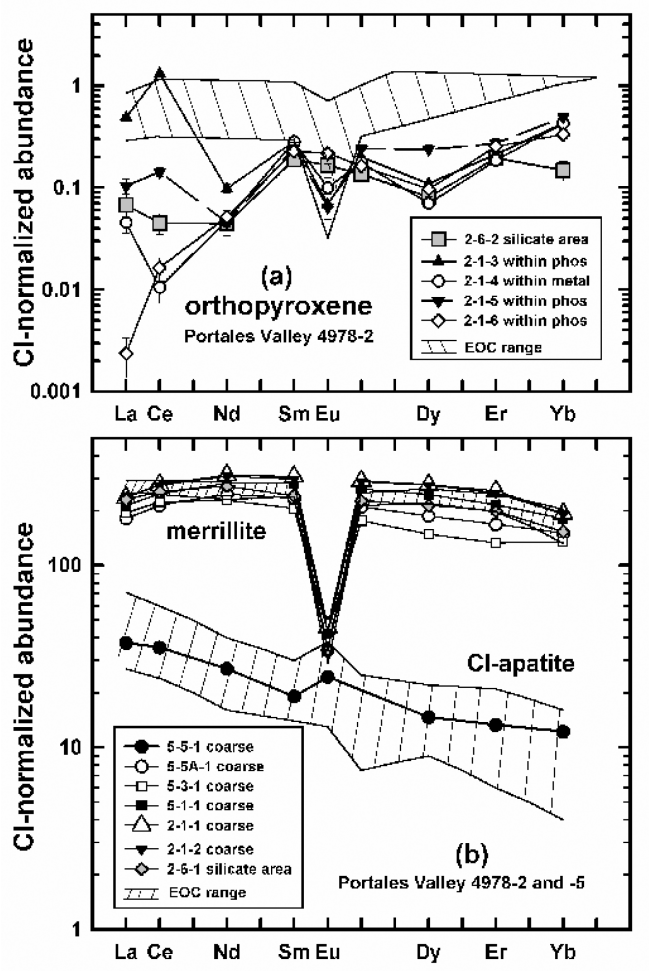

Fig. 7. CI-normalized abundances of some REE in a) orthopyroxene and b) phosphate in Portales Valley, based on SIMS analyses. For comparison, ranges show measured compositions in equilibrated ordinary chondrites (EOC) orthopyroxene (Curtis and Schmitt 1979; Allen and Mason 1973) and EOC phosphate (Curtis and Schmitt 1979; Crozaz et al. 1989). REE abundances in merrillite and CI-apatite in Portales Valley overlap those in metamorphosed H chondrites; REE abundances in orthopyroxene from Portales Valley appear somewhat low compared to the abundances reported from H chondrites. The CI chondrite abundances of Anders and Grevesse (1989) were used for normalization.

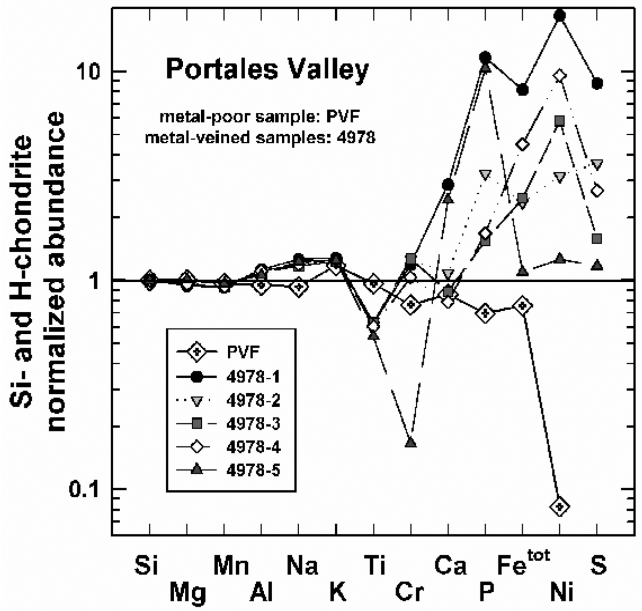

Fig. 8. Major-element abundances normalized to Si and to average H chondrites in metal-poor sample PVF and for various sections of metal-veined samples from AMNH 4978. Portales Valley data are from Table 6; data for H chondrites are from Jarosewich (1990). Si-normalized abundance ratios for some elements (e.g., Ca, P, Fe, Ni, S) in some samples depart greatly from average H chondrite values, whereas those for some elements (e.g., Mg, Mn, Al) in all samples resemble those in H chondrites.

As to be depleted in the coarse metal relative to H chondrites, but the opposite was found by Rubin et al. (2001). These data suggest that coarse metal in PV has a spatially variable composition.

A high abundance of Ga in PV coarse metal was found both in this study (Table 7) and that of Rubin et al. (2001), although different concentrations were measured (~30 and ~18 ppm, respectively). The values for both measurements are significantly higher than for typical metal in H chondrites (14 ± 2 ppm; average and standard deviation of data given by Chou et al. 1973; Rambaldi 1977; Kong et al. 1995) and are similar to that found in metal from IIE iron meteorites (25 ± 3 ppm) (Wasson and Wang 1986; Ebihara et al. 1997). High Ga abundances in chondritic metal can be produced by a high degree of thermal metamorphism or by shock (Chou and Cohen 1973), presumably by transfer of Ga from silicates to metal during heating. Thus, high Ga abundances in PV metal imply an unusual history for the metal.

In summary, the bulk composition in significant volumes of PV is not H-chondritic, although there is an overall resemblance to H chondrites. This is true both for the non-metallic and metallic fractions of the meteorite.

DISCUSSION

Chemical Fractionations and Mixing Models

Simple mixing models were devised to test whether bulk-chemical variations in lithophile and siderophile element abundances (see Bulk Composition section) could be explained by spatial variations in phosphate and metal abundance. As previously noted, the abundances of these phases vary widely within PV (see Modal Composition section), and variations in bulk trace element abundances of lithophile elements are suggestive of phosphate control (see Bulk Composition section).

Figure 10 shows results of a mixing model for REE in which variable amounts of merrillite are added to or subtracted from an average H chondrite containing 0.4 wt% merrillite, compared to the measured abundances in various

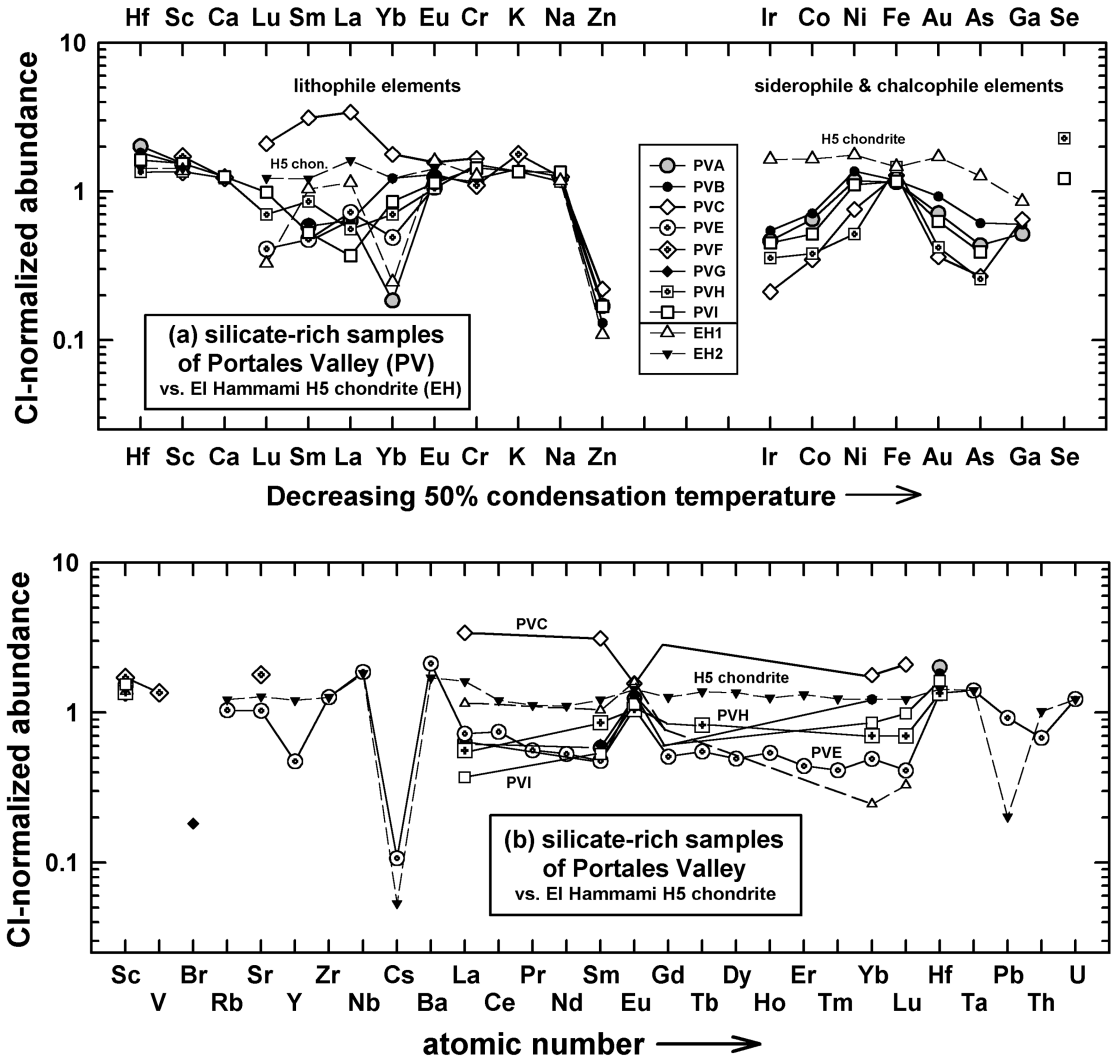

Fig. 9. CI-normalized abundances of various splits of Portales Valley. a) Lithophile and siderophile-chalcophile element abundances in silicate-rich samples of Portales Valley (PV samples) are compared to the El Hammami Mountains H5 chondrite (EH1 and EH2 samples), with elements arranged according to decreasing 50% condensation temperatures (Wasson 1985). Data are from Tables 7 and 8. The CI chondrite abundances of Anders and Grevesse (1989) were used for normalization. b) Same as (a), but for an expanded number of incompatible lithophile elements, with elements arranged according to atomic number.

splits. This model assumes that only the abundance of merrillite is varying and that the composition of the remaining non-merrillite fraction is constant. The shapes of the predicted and observed patterns are similar, including the sizes of Eu anomalies (Fig. 10), suggesting that variations in the abundances of merrillite can largely account for the chemical variations seen in PV. Compared to an average H chondrite with ~0.4 wt% merrillite, sample PVC could be ~2–3× enriched, whereas the remaining samples could be ≥2–3× depleted (Fig. 10). The lack of detailed agreement between the calculated and observed abundances is easily explained if other phases besides merrillite have non-chondritic proportions. For example, comparatively low HREE abundances in samples PVE, PVH, and PVC compared to the models (Fig. 10) could indicate a low content of an HREE-rich phase such as clinopyroxene, which is widely depleted in PV compared to H chondrites (see Modal Composition section).

Figure 11 compares measured siderophile element abundances in different samples with a simple model in which various amounts of average H chondrite metal are mixed with average H chondrite non-metallic fraction, using as constraints the composition of metal and silicates in H chondrites and the bulk composition of H chondrites (Chou et al. 1973; Rambaldi 1977; Kong et al. 1995; Wasson and Kallemeyn 1988). This model tests whether variations in siderophile element abundances are caused by variations in metal abundance alone, assuming that metal maintains a constant H-chondrite-like composition. The model can explain the pattern observed for the reference H5-chondrite El

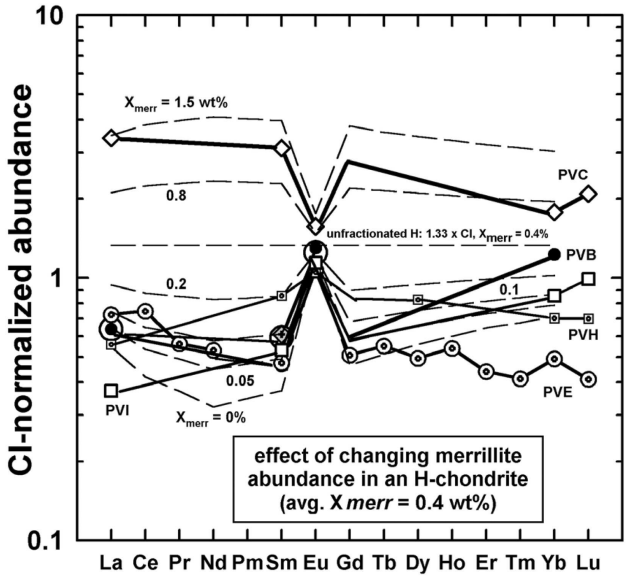

Fig. 10. CI-normalized abundances for REE in various splits of Portales Valley (Tables 7 and 8) are compared to a model in which merrillite is mixed in various proportions in an otherwise chondritic assemblage. The model assumes that merrillite with a composition identical to the average found in this study (Table 5a) is added to or subtracted from an H chondrite assemblage that originally has unfractionated REE abundances of 1.33 × CI chondrites and 0.4 wt% merrillite. The CI chondrite abundances of Anders and Grevesse (1989) were used for normalization. REE abundance variations in PV can be explained primarily by variations in the amount of merrillite.

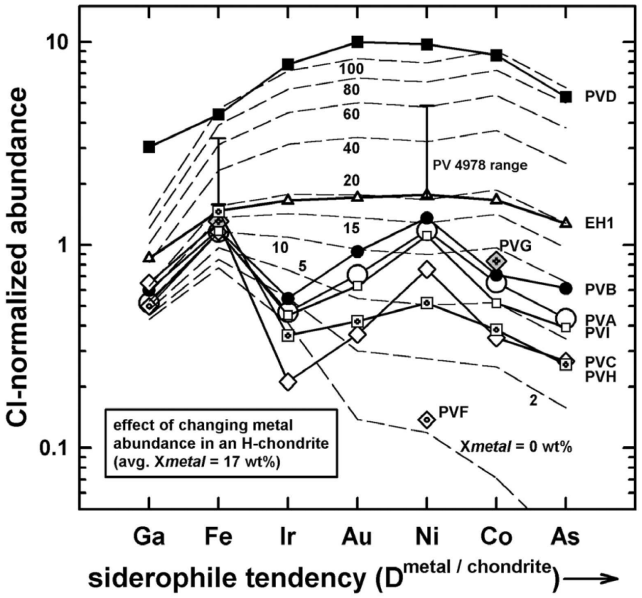

Fig. 11. CI-normalized abundances for siderophile elements in various splits of Portales Valley (PV) and in El Hammami H5 chondrite (EH1) are compared to a model in which metal of average H chondrite composition is mixed in variable proportions in an otherwise chondritic assemblage. Measured compositions for PV and EH1 are taken from Tables 2, 7, and 8. The model assumes that metal of average composition in H4-6 chondrites (Chou et al. 1973; Rambaldi 1977; Kong et al. 1995) is added to or subtracted from an H chondrite assemblage with 17 wt% metal and the average bulk composition found in H chondrites (Wasson and Kallemeyn 1988). The CI chondrite abundances of Anders and Grevesse (1989) were used for normalization. Siderophile element abundances in PV cannot be explained by variations in the amount of metal with chondritic composition.

Hammami EH1 sample if it contains just under ~20 wt% H-chondrite-like metal, which is similar to the average amount of metal (~17 wt%) in H chondrites (Fig. 11). The model cannot explain the high Ga abundances in EH1, which may indicate that Ga is enriched in El Hammami relative to typical H chondrites. Based on Fe and Ni abundances, the mixing model also is consistent with the observed range in metal abundance for various sections of PV 4978 (~20–60 wt% in AMNH 4978, corresponding to ~8–44 vol% metal) (Table 2).

However, the metal-silicate mixing model does not reproduce the pattern for siderophile elements in silicate-rich samples of Portales Valley (PVA, PVB, PVC, PVI, or PVH), and it also does not completely agree with the pattern observed for the coarse metal separate (PVD). The coarse metal contains more Au, Ni, and Ga than predicted for 100% H chondrite metal (Fig. 11). Moreover, the mixing model cannot account for the highly fractionated pattern observed in silicate-rich samples (Fig. 11). Although Ga and Fe abundances in bulk silicate-rich samples cannot be used as strict indicators of metal composition owing to their presence in phases other than metal (such as silicate and sulfide), consistently low Ir/Ni, Au/Ni, Co/Ni, and As/Ni values obtained for silicate-rich areas (Fig. 11) indicate that fine-grained metal in PV has a non-chondritic composition. Evidently, both fine- and coarse-grained metal in PV is chemically fractionated compared to that in H chondrites.

Textural Evidence for Melting of Metal

There is good textural evidence that some of the metal and troilite in Portales Valley was melted. Metal-veining textures (Fig. 1a) imply that metal was substantially molten and that this metal sometimes entrained silicate clasts (Pinault et al. 1999; Scott and Pinault 1999; Ruzicka et al. 1999a; Rubin and Ulff-Møller 1999; Rubin et al. 2001). Widmanstätten textures and Ni zoning patterns imply that coarse metal in veins consisted of large taenite parent crystals at high temperature, which exsolved at a lower temperature to form kamacite (Kring et al. 1999a, 1999b; Pinault et al. 1999; Ruzicka et al. 1999b; Reisener and Goldstein 2003); the large size of such metal grains is consistent with idea that metal nucleated and grew from a liquid. Rubin et al. (2001) found evidence with high-resolution X-ray computerized tomography for apparent flotation of smaller silicate clasts within coarser metal veins, implying not only that metal was significantly molten, but that movement of metal and silicate occurred over an extended time period in the presence of a non-negligible gravity field.

Table 6. Major element bulk composition of metal-veined (AMNH 4978) and silicate-rich (PVF) portions of Portales Valley, compared to average H chondrite. n.a. = not analyzed.

	AMNH 4978[a]						PVF[b]	H chondrite[c]
	-1	-2	-3	-4	-5	avg.		
wt%								
SiO_2	10.8	25.4	25.1	17.6	34.1	21.5	39.77	36.73
TiO_2	0.02	0.05	0.05	0.03	0.06	0.04	0.13	0.12
Al_2O_3	0.71	1.64	1.60	1.13	2.12	1.37	2.20	2.14
Cr_2O_3	0.18	0.45	0.45	0.26	0.08	0.28	0.43	0.51
FeO	2.66	6.45	6.30	4.42	9.12	5.50	[28.5]	10.55
MnO	0.08	0.20	0.20	0.14	0.28	0.17	0.33	0.31
MgO	6.43	15.6	15.2	10.7	22.1	13.3	25.13	23.31
CaO	1.44	1.30	1.05	0.66	3.85	1.56	1.61	1.74
Na_2O	0.31	0.71	0.67	0.48	0.96	0.60	0.85	0.84
K_2O	0.04	0.08	0.08	0.06	0.11	0.07	0.12	0.09
P_2O_5	0.91	0.60	0.29	0.22	2.54	0.85	0.20	0.27
Fe	62.2	38.9	40.3	54.2	20.4	45.1	–	15.43
Ni	9.12	3.68	6.64	7.67	1.98	6.16	0.15	1.71
S	5.03	4.93	2.12	2.52	2.14	3.43	n.a	1.96
Cl	0.10	0.01	0.01	0.00	0.24	0.06	n.a.	n.a.
C	n.a	n.a	n.a	n.a	n.a	n.a	n.a	0.11
Total	100.03	100.03	100.06	100.09	100.08	99.99	99.42	99.23
Atomic								
Mg/Si	0.891	0.913	0.904	0.907	0.964	0.921	0.9418	0.9460 ± 0.0097
Al/Si	0.077	0.0759	0.0752	0.0761	0.0732	0.0754	0.0652	0.0687 ± 0.0047
Ca/Si	0.144	0.0548	0.0449	0.0403	0.121	0.0776	0.0434	0.0506 ± 0.0027
P/Si	0.072	0.020	0.010	0.011	0.063	0.033	0.0043	0.0062 ± 0.0009
Na/Si	0.056	0.054	0.052	0.053	0.055	0.054	0.041	0.044 ± 0.005
Fe^{sil}/Si^d	0.206	0.212	0.210	0.211	0.224	0.214	–	0.2406 ± 0.0411
Fe^{met}/Si^d	6.22	1.65	1.73	3.32	0.643	2.26	–	0.5523 ± 0.0589
Fe^{tot}/Si^d	6.42	1.86	1.94	3.53	0.866	2.47	0.599	0.7929 ± 0.0462
S/Si	0.876	0.363	0.158	0.269	0.118	0.299	–	0.100 ± 0.010

[a]Determined by modal reconstruction. Combines modal data (Table 2) with average phase compositions (Tables 3–4) and phase densities (Gaines et al. 1997). Low-Ni and high-Ni metal in Table 2 is assumed to correspond to average kamacite and taenite, respectively.

[b]Determined by XRF analysis (Table 8). All iron as FeO.

[c]Mean water-free H chondrite (Jarosewich 1990), excluding weathered samples. Numbers after "±" refer to standard deviation of the mean.

[d]Fe^{sil} = iron in silicate; Fe^{met} = iron in metal and sulfide; Fe^{tot} = total iron.

Melting and Crystallization Models for Siderophile Elements

Here we test whether melting and crystallization models can explain the fractionated and spatially variable compositions of metal in PV (see Chemical Fractionations and Mixing Models section). Our models assume that Portales Valley was derived from an H chondrite protolith. The proportion of S in the metallic (Fe + Ni + S) fraction of bulk H chondrites was determined by taking the average composition of unweathered H chondrite falls (Jarosewich 1990), and the abundance of trace elements in H chondrite metal was averaged from literature data (Chou et al. 1973; Rambaldi 1977; Kong et al. 1995). These data sets were merged to obtain a representative composition of the metallic fraction in H chondrites (Table 9).

Modelled compositions of metallic liquids and solids were compared to observed compositions of coarse vein metal and finer-grained metal in silicate-rich areas using Ni-normalized data. As a significant amount of Ga and Fe in chondrites is contained in the silicate fraction, measured Ga/Ni and Fe/Ni values cannot be used as much of a constraint for fine-grained metal in silicate-rich samples. Additionally, Ga/Ni and Fe/Ni do not provide good constraints for the coarse metal analyzed by us (sample PVD). This is because in this sample, the Fe content was calculated by difference (Table 7) and the Ga concentrations appear too high to have been derived from an H chondrite starting composition by solid-liquid metal partitioning alone and may instead reflect an unusual thermal history (see Bulk Composition section). Thus, the major model constraints for both fine and coarse metal are provided by Ir/Ni, Au/Ni, Co/Ni, and As/Ni.

Abundances of siderophile elements were calculated using standard melting and crystallization equations (e.g., Rollinson 1993) based on solid metal/liquid metal partition coefficients (D values). Composition-dependent D values for Ni, Co, Au, Ir, and Ga were determined using the formulations of Chabot and Jones (2003); similar results were

obtained using the somewhat different formulations of Jones (1995) and Liu and Fleet (2001). The equilibrium Fe-Ni-S ternary phase diagram of Hsieh et al. (1987) and the well-constrained equilibrium Fe-S phase diagram of Hansen and Anderko (1958) and Kubaschewski (1982) were used as guides to constrain the S content of metallic melts and the corresponding metallic melt fractions and temperatures. The S content of H chondrite melts was calculated assuming that all sulfur partitions into whatever metallic melt is present, according to the mass balance expression:

$$X_S = 0.1412 + (1 - F_L) \cdot 0.4436 \quad (1)$$

where X_S = atom fraction of S in the metallic melt and F_L = fraction of metallic liquid in the Fe + Ni + S system. This expression indicates that for a total melt ($F_L = 1$), $X_S = 0.1412$, which corresponds to an H chondrite composition, whereas $X_S = 0.44$ for a Fe-S eutectic melt fraction at 988 °C (Hansen and Anderko 1958; Kubaschewski 1982), corresponding to $F_L = 0.326$. The addition of small amounts of Ni to the Fe-S system changes melting relations only slightly, yielding a Fe-Ni-S eutectic temperature at low pressure of ~943 °C (Usselman 1975). As the abundances of all other modelled elements in the metallic system were determined, the amount of iron in solid and liquid metal was calculated by difference.

Various models were examined. These include equilibrium "batch" melting; batch melting followed by equilibrium crystallization of separated liquids; batch melting followed by fractional crystallization; equilibrium melting followed by in situ crystallization of the resulting liquids (Langmuir 1989); and equilibrium melting with incomplete separation of melt from solid. Example results for some of the best-fit cases of each of these models are shown in Table 9 and are discussed below. Of these models, equilibrium melting with incomplete separation of melt from solid can best explain the data for Portales Valley.

Equilibrium Batch Melting

This model assumes partial melting of the metallic fraction in order to produce metallic melts that separate all at once from the residual solid in a "batch." The results of these models suggest that metal in PV cannot be a residue of a partial melting event, as the predicted values of the Ir/Ni, Au/Ni, Co/Ni, and As/Ni in solid metal all tend to be high (>H chondrites), opposite to what is observed (Table 9). Melt compositions produced in this process also do not provide a good match, in that calculated Ir/Ni values are far too low compared to Au/Ni, Co/Ni, and As/Ni (Table 9).

Batch Melting Followed by Equilibrium Crystallization of the Separated Liquids

This model tests whether equilibrium crystallization of a separated batch liquid can account for metal in PV. For this model, no combination of melting and crystallization conditions was found that results in a particularly good match between either the model liquids or solids to either the coarse or fine metal in PV. Table 9 shows what is probably the best case for a solid that somewhat resembles PV metal except for having too much Co and As.

Batch Melting Followed by Fractional Crystallization of the Separated Liquids

This model is similar to the previous one, except that fractional crystallization is assumed to occur. Final liquids in this model are unpromising analogues to PV metal, as they tend to be enriched in Au and As except at lower melt fractions and Ir becomes impoverished in these low-melt fractions. Final solids provide more reasonable matches to PV metal when both the degree of melting is extensive and the amount of subsequent crystallization is small. Table 9 shows one of the more promising cases which is, however, too high in Co/Ni.

Equilibrium Melting Followed by In Situ Crystallization of the Resulting Liquid

Equations for this type of crystallization were devised by Langmuir (1989) to model a situation thought to occur in magma chambers on Earth, in which crystallization occurs in a "crystal mush" zone along magma chamber boundaries and residual liquid is expelled from the mush zone as solidification proceeds. For this model, we assumed two values (0.5, 0.9) for the parameter *f*, where *f* represents the fraction of magma (0–1) allocated to the mush zone which is returned to the main magma body. An optimized case for a final liquid is shown in Table 9; this provides the worst match to PV for any of the models shown.

Equilibrium Melting with Incomplete Separation of Residual Metal from Metallic Liquids

This is similar to a batch melting model, except that liquids do not fully separate from solids and so no distinct liquid batch is produced. Solids and liquid are always in direct contact and in equilibrium. Cases examined include partial melting with melt fractions ranging from $F_L = 0.9$ to 0.33 and metal + liquid mixtures containing 5–95% solid metal. With this model, the trace element content of PV metal can be successfully explained as having formed by the production of metallic melts generated from an H-like precursor at relatively low temperatures.

Figure 12 shows results for various solid-liquid mixtures produced by equilibrium melting at $F_L = 0.33$, 0.40, and 0.5. At $F_L = 0.33$ (a eutectic melt), the H-normalized Ir/Ni, Au/Ni, Co/Ni, and As/Ni values calculated for a solid-liquid metal mixture containing ~20–40% solid agrees with the observed composition of fine metal in PV, and a mixture containing ~40–80% solid agrees with the composition of coarse metal in PV (Fig. 12a, Table 9). Thus, metal in both vein and silicate-

Table 7. Bulk composition of various splits of the Portales Valley meteorite and of the El Hammami Mountains H5 chondrite, analyzed by the INAA method. PVD is a sample of coarse vein metal; other PV samples represent metal-poor, silicate-rich material (Table 1). Uncertainties (see text) are given in parentheses. n.d. = not determined.

		Portales Valley							El Hammami
		PVA	PVB	PVC	PVD	PVG	PVH	PVI	EH1
Na	mg/g	6.2 (0.4)	6.1 (0.4)	6.0 (0.4)	0.1 (0.03)	6.3 (0.1)	5.86 (0.12)	6.76 (0.14)	5.9 (0.4)
K	mg/g	n.d.	n.d.	n.d.	n.d.	0.79 (0.54)	0.76 (0.09)	0.76 (0.11)	n.d.
Ca	wt%	n.d.	n.d.	n.d.	n.d.	n.d.	1.14 (0.20)	1.17 (0.14)	n.d.
Sc	µg/g	9.02 (0.27)	8.82 (0.26)	7.79 (0.23)	0.36 (0.09)	9.1 (0.09)	7.90 (0.16)	8.94 (0.18)	8.06 (0.24)
Cr	µg/g	3080 (310)	2960 (296)	4430 (440)	29 (4)	3233 (12)	4040 (800)	3830 (800)	3410 (340)
Fe	wt%	22.0 (1.1)	22.6 (1.1)	24.6 (1.2)	88.9[a]	25.1 (0.5)	27.8 (0.6)	22.2 (0.4)	28.1 (1.4)
Co	µg/g	328 (16)	358 (18)	175 (9)	4320 (220)	419 (8)	192 (4)	260 (5)	831 (42)
Ni	wt%	1.30 (0.16)	1.51 (0.18)	0.84 (0.06)	10.67 (0.07)	n.d.	0.57 (0.011)	1.219 (0.024)	1.93 (0.13)
Zn	µg/g	53 (8)	41 (6)	69 (10)	n.d.	56 (14)	53 (6)	53 (7)	34 (5)
Ga	µg/g	5.2 (1.3)	6.0 (1.5)	6.5 (1.6)	30.4 (7.6)	n.d.	n.d.	n.d.	8.6 (2.2)
As	µg/g	0.81 (0.10)	1.14 (0.08)	0.50 (0.09)	10.0 (0.5)	1.44 (0.33)	0.48 (0.11)	0.73 (0.15)	2.37 (0.12)
Se	µg/g	n.d.	n.d.	n.d.	n.d.	n.d.	42.5 (2.7)	22.6 (1.5)	n.d.
Sb	ng/g	n.d.	n.d.	n.d.	n.d.	n.d.	<36	34 (15)	n.d.
La	ng/g	150 (40)	150 (30)	800 (80)	n.d.	n.d.	131 (15)	87 (14)	270 (30)
Sm	ng/g	86 (7)	68 (7)	460 (23)	n.d.	90 (10)	126 (5)	78 (7)	150 (10)
Eu	ng/g	70 (10)	73 (7)	88 (7)	n.d.	n.d.	59 (4)	64 (5)	90 (20)
Tb	ng/g	n.d.	n.d.	n.d.	n.d.	n.d.	30 (13)	<45	n.d.
Yb	ng/g	30 (20)	200 (50)	290 (50)	n.d.	n.d.	114 (28)	139 (30)	40 (20)
Lu	ng/g	n.d.	n.d.	51 (11)	n.d.	n.d.	17 (7)	24 (4)	8 (3)
Hf	ng/g	210 (40)	190 (40)	n.d.	n.d.	n.d.	140 (50)	170 (40)	n.d.
Ir	ng/g	225 (23)	263 (26)	102 (10)	3730 (370)	n.d.	172 (5)	217 (6)	793 (79)
Au	ng/g	100 (20)	130 (20)	n.d.	1400 (200)	n.d.	58.8 (1.9)	88.0 (2.7)	240 (40)

[a]Calculated by difference. The apparent value (83.6 wt%) is unreliable due to large extrapolation from composition of standard.

Table 8. Bulk composition of various splits of Portales Valley and of the El Hammami Mountains H5 chondrite as determined by ICPMS (samples PVE and EH2) and XRF (sample PVF) methods. PVE and PVF are samples of metal-poor, silicate-rich material. Uncertainties (see text) are given in parentheses. n.d. = not determined.

		Portales Valley		El Hammami
		PVE	PVF	EH2
Na	mg/g	n.d.	6.3 (0.04)	n.d.
Mg	wt%	n.d.	15.15 (0.57)	n.d.
Al	mg/g	n.d.	11.6 (0.03)	n.d.
Si	wt%	n.d.	18.59 (0.04)	n.d.
P	mg/g	n.d.	0.886 (0.005)	n.d.
K	mg/g	n.d.	0.996 (0.069)	n.d.
Ca	wt%	n.d.	1.15 (0.005)	n.d.
Sc	µg/g	8.9 (0.9)	10 (2)	8.3 (0.9)
Ti	mg/g	n.d.	0.749 (0.004)	n.d.
V	µg/g	n.d.	77 (5)	n.d.
Cr	mg/g	n.d.	2.926 (0.176)	n.d.
Mn	mg/g	n.d.	2.53 (0.04)	n.d.
Fe	wt%	n.d.	22.15 (0.18)	n.d.
Ni	mg/g	n.d.	1.524 (0.091)	n.d.
Ga	µg/g	n.d.	5 (0.5)	n.d.
Rb	µg/g	2.4 (0.3)	n.d.	2.8 (0.3)
Sr	µg/g	8 (0.4)	14 (0.05)	10 (0.5)
Y	µg/g	0.74 (0.04)	n.d.	1.89 (0.10)
Zr	µg/g	5	n.d.	5
Nb	µg/g	0.46	n.d.	0.45
Cs	ng/g	20 (5)	n.d.	10 (2)
Ba	µg/g	5.0 (0.3)	n.d.	4.0 (0.3)
La	ng/g	170 (11)	n.d.	380 (23)
Ce	ng/g	450 (18)	n.d.	730 (29)
Pr	ng/g	50 (2)	n.d.	100 (4)
Nd	ng/g	240 (12)	n.d.	500 (24)
Sm	ng/g	70 (4)	n.d.	180 (11)
Eu	ng/g	60 (4)	n.d.	80 (5)
Gd	ng/g	100 (4)	n.d.	250 (10)
Tb	ng/g	20 (1)	n.d.	50 (2)
Dy	ng/g	120 (5)	n.d.	330 (13)
Ho	ng/g	30 (1)	n.d.	70 (3)
Er	ng/g	70 (3)	n.d.	210 (9)
Tm	ng/g	10 (0.4)	n.d.	30 (1)
Yb	ng/g	80 (3)	n.d.	200 (6)
Lu	ng/g	10 (1)	n.d.	30 (2)
Hf	ng/g	140 (8)	n.d.	150 (9)
Ta	ng/g	20 (4)	n.d.	20 (4)
Pb	µg/g	2.28 (0.46)	n.d.	0.5 (0.1)
Th	ng/g	20	n.d.	30
U	ng/g	10 (3)	n.d.	10 (3)

rich areas can be modelled as representing a mixture of solid and liquid portions produced under the same melting condition.

With forty percent partial melting, there is less agreement between the model and observations (Fig. 12b). Under these conditions, the fine metal fraction in PV could correspond to ≤5% entrained solid based on Au/Ni, Co/Ni, and As/Ni values, and ~20–40% entrained solid based on Ir/Ni. The proportion of solid metal in the coarse veins in PV would be higher, perhaps ~20–60%. With fifty percent partial melting, the model clearly fails (Fig. 12c). As the degree of melting increases, Co/Ni, As/Ni, and Au/Ni values increase and do not permit good matches to the observations. Essentially, the degree of fractionation diminishes as the degree of melting increases.

Summary and Implications of Modelling Results

It appears that a model involving partial melting and incomplete separation of solid and liquid metal best accounts for the composition of metal observed in Portales Valley.

Table 9. Model calculations for abundances of siderophile elements and S compared to observed values in Portales Valley. Values are normalized to the average composition of the metallic system in H chondrites (taken to be 82.55 wt% Fe, 8.59 wt% S, 7.49 wt% Ni, 1.36 wt% Co, 4.22 ppm Ga, 1.04 ppm Ir, 0.348 ppm Au, 3.50 ppm As). F_L = fraction of liquid after step. Values in parentheses for Portales Valley reflect 1-σ measurement uncertainty (coarse vein metal) and standard deviation for multiple analyses (fine metal + sulfide in silicate-rich areas). Iron and Ga values in Portales Valley "fine metal" fraction are upper limits, as some of these elements reside in silicates. See text for explanation and discussion of models.

		H-chondrite-normalized values (wt)						
Model	Phase	S/Ni	Ga/Ni	Fe/Ni	Ir/Ni	Au/Ni	Co/Ni	As/Ni
Batch melting (F_L = 0.40)	liquid	4.63	0.135	1.13	0.005	0.771	0.489	0.727
	solid	0	1.29	0.921	1.33	1.08	1.17	1.09
Batch melting (F_L = 0.8), then equilibrium crystallization (F_L = 0.7)	liquid	2.83	0.405	0.944	0.027	1.30	0.685	1.29
	solid	0	1.47	0.905	0.889	0.919	1.23	0.935
Batch melting (F_L = 0.9), then fractional crystallization (F_L = 0.8)	liquid	1.76	0.732	0.946	0.086	1.24	0.841	1.25
	solid	0	1.41	1.01	0.732	0.566	1.24	0.563
Equilibrium melting (F_L = 0.4), then in situ crystallization (F_L = 0.9, f = 0.5)	liquid	5.41	0.126	1.09	0.001	0.736	0.162	0.692
	solid	0	4.12	0.727	4.57	2.44	0.562	2.63
Equilibrium melting (F_L = 0.326)	mixture 60% solid	2.41	0.738	1.08	0.722	0.852	0.826	0.839
Equilibrium melting (F_L = 0.326)	mixture 30% solid	4.22	0.398	1.19	0.361	0.659	0.600	0.630
Portales Valley	coarse metal	~0	1.74 (0.49)	~0.811 (0.105)	0.878 (0.137)	0.993 (0.183)	0.781 (0.100)	0.705 (0.091)
Portales Valley	fine metal	>1	<3.21 (1.09)	<2.50 (1.23)	0.477 (0.150)	0.605 (0.107)	0.482 (0.089)	0.515 (0.074

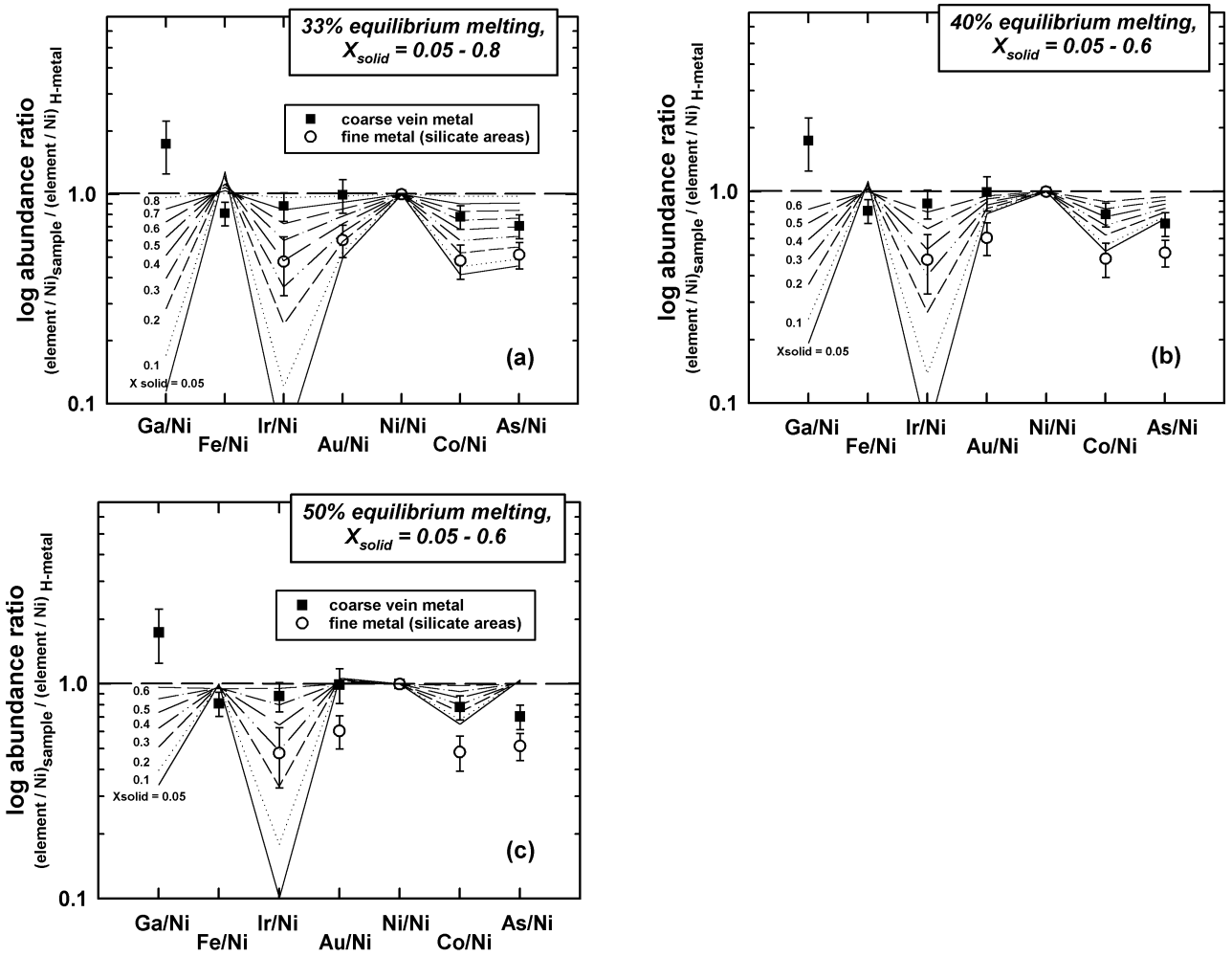

Fig. 12. Ni-normalized and H-chondrite-normalized siderophile element abundances in PV are compared to a model in which solids and melt produced by equilibrium melting are incompletely separated. PV data are from Tables 7 and 8; average H chondrite compositions are based on Jarosewich (1990); Chou et al. (1973); Rambaldi (1977); and Kong et al. (1995). Error bars for the coarse vein metal (PVD) represent analytical uncertainty; errors bars for fine-grained metal in PV silicate-rich samples reflect the standard deviation of the mean composition. a) 33% equilibrium melting (eutectic conditions) in the Fe + Ni + S system, corresponding to T ~940–990 °C. b) 40% equilibrium melting, T ~1150 °C. c) 50% equilibrium melting, T ~1300 °C. The observed compositions are matched for mixtures produced at eutectic or near-eutectic melting conditions (~33% to as much as 40% melting), with higher proportions of solid in the coarse veins than in silicate-rich areas. See text.

Besides providing the best fit to the observations among all the models examined, this model is one of the simplest and most physically plausible. The model has the advantage that the composition of metal in both coarse veins and in silicate-rich areas can be established by the same process, although different proportions of solid and liquid in different areas are implied. Incomplete separation of melt from solid is not unexpected in low-gravity objects, especially at low degrees of partial melting in which the high proportion of solid inhibits the ability of liquid and solid to separate. At the near-eutectic conditions inferred, most of the metal would be solid.

It appears that the degree of metallic partial melting was less than fifty percent—and probably less than forty percent—at the time the composition of the metal was established (Fig. 12). The model results do not rule out the possibility of higher melting fractions; rather, they constrain the overall closure temperature for equilibrium between solid and liquid metal. For an H chondrite starting composition, a metallic melt fraction of ≤40% constrains the temperature to about 940–1150 °C (Hansen and Anderko 1958; Usselman 1975; Hsieh et al. 1987). These temperatures are much lower (≥1480 °C) than those inferred by Rubin et al. (2001), which was based on the overall composition of coarse, S-poor metal and textural evidence that metal was liquefied. However, if metal in the veins did not form all at once but rather grew to replace liquid, as argued here, the high temperature estimate would be erroneous.

For temperatures of about 940–1150 °C, it is possible that the non-metallic fraction of Portales Valley was partly molten. Heating experiments of L chondrite starting material

at about 15 Kbar produces silicate melt at about 1100 °C, with lower melting temperatures expected at lower pressures (Takahashi 1983). Equilibrium melting experiments at low pressure with H and LL ordinary chondrites under fO_2 values close to the IW buffer suggest that about 10–13 wt% and about 15–20 wt% of the silicate fraction will be molten at temperatures of about 1120–1170 °C and about 1200 °C, respectively (Jurewicz et al. 1995). This implies a maximum degree of silicate partial melting in PV of about 13% at the time solid and liquid metal compositions were fixed. Plagioclase is fully molten even at the lowest temperatures investigated by Jurewicz et al. (1995), and plagioclase, phosphate, and clinopyroxene melt completely at 1200 °C within 1–10 hours in experiments with an L chondrite (Feldstein et al. 2001). Thus, it is possible that some or all of the plagioclase, phosphate, and clinopyroxene were melted in Portales Valley.

Origin of Troilite-Rich Silicate Areas and Troilite Veins

Based on the results of models described above (see Melting and Crystallization Models for Siderophile Elements section), which provide good agreement to the observations for PV, silicate-rich areas that ultimately crystallized to fine-grained metal should have incorporated a higher proportion of liquid metal than the coarse veins, including more sulfur (e.g., S/Ni ~4.7 for the fine metal fraction, ~2.7 for the coarse metal fraction; Table 9). Upon solidification, this excess S would be expected to lead to troilite formation. In agreement with this, troilite in PV is indeed concentrated in silicate-rich areas. Modelling results suggest that the vein metal was ~40–80% solid at the time of last equilibration. This implies that ~20–60% of S-bearing liquid metal must have been expelled from the coarse veins, and probably moved into adjacent silicate-rich areas, before Portales Valley attained its present configuration of sulfide-free coarse veins. Textural evidence for this process includes the presence of thinner troilite and metal veins that interconnect to coarse veins (Figs. 1b and 1d), which probably served as conduits for metallic liquid that was pushed out of coarse veins. The interfaces between troilite and metal veins are also suggestive of later crystallization of troilite (see Overall Petrography of Portales Valley section), which is consistent with this model.

An overall movement of liquid from coarse veins to surrounding areas agrees with the conclusions of Pinault et al. (1999). According to these researchers, the silicate-rich matrix of Portales Valley behaved effectively as a sponge, absorbing S-rich melt as large metal crystals grew within the veins. Rubin et al. (2001) proposed an analogous model, in which pores within the silicate-rich fraction of Portales Valley were filled with S-rich vapor, which reacted with Fe vapor or metal to form troilite. In both cases, the metal in silicate-rich areas completed crystallization after the coarse vein metal, in agreement with our results.

Origin of Large Graphite Nodules

At least two distinct graphite nodules up to a few cm across have been identified in Portales Valley so far, both embedded within coarse vein metal (see Overall Petrography of Portales Valley section). Coarse graphite in general, and nodules in particular, are absent in other ordinary chondrites. H chondrites contain ~0.11 wt% carbon on average (Jarosewich 1990) and to produce cm-sized graphite nodules from an H chondrite precursor requires that C must have been scavenged from large volumes and concentrated locally.

According to the equilibrium Fe-C phase diagram (Massalski et al. 1986), a eutectic in the Fe-C system between taenite and graphite occurs at ~1150 °C. This indicates that liquid metal could have co-crystallized graphite and taenite if temperatures reached this high. This is the upper temperature limit estimated for the equilibrium established between solid and liquid metal based on siderophile element abundances in metal (see Melting and Crystallization Models for Siderophile Elements section). In reality, however, graphite could have crystallized from liquid metal at a lower temperature in PV, as the addition of other components (Ni, S, P, etc.) to a metallic melt would lower the actual eutectic temperature compared to the Fe-C system (e.g., Doan and Goldstein 1969). It therefore seems likely that temperatures in PV were sufficiently high to place C in a metallic liquid and that the graphite nodules in PV formed by crystallization of graphite from this liquid. The formation of coarse graphite, as opposed to smaller distributed grains in metal, implies there was an additional driving force favoring the formation of large grains—perhaps a minimization of surface energy or a tendency for C-rich liquids to immiscibly separate from C-poor liquids.

Eutectic crystallization of graphite and FeNi metal is entirely consistent with the observed textures of the nodules, which show evidence for contemporaneous formation of graphite and coarse FeNi metal (see Overall Petrography of Portales Valley section). The co-crystallization of metal and graphite from C-bearing liquids is probably the same process that produced graphite nodules in iron meteorites. The presence of coarse graphite nodules within coarse metal vein areas in PV can be taken as further evidence that such veins were significantly molten at one time. The high proportion of kamacite associated with the graphite (see Overall Petrography of Portales Valley section) can be explained by preferential nucleation and growth of kamacite from taenite grain boundaries under subsolidus conditions, the same process that was likely responsible for the formation of swathing kamacite on coarse veins in PV (Fig. 1c).

Petrogenesis of Coarse Phosphate: Igneous or Metamorphic?

Both igneous and metamorphic processes were probably important in establishing the textural and chemical properties

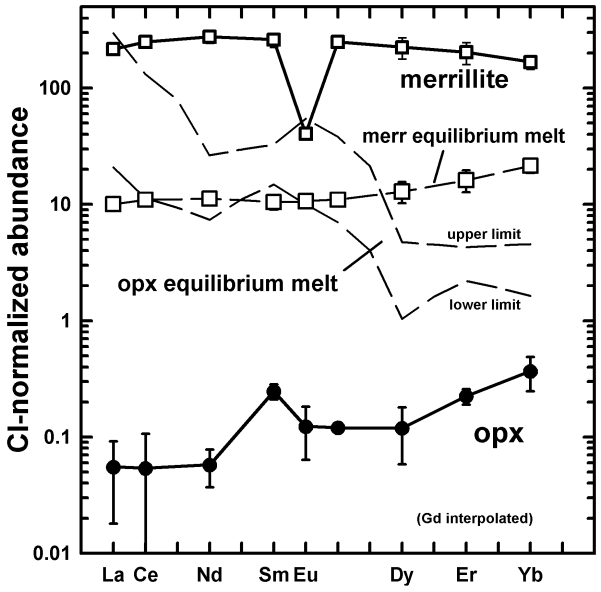

Fig. 13. Measured average REE abundances in merrillite and orthopyroxene (Table 5) are compared to the composition of melt that would be in equilibrium with these phases. The calculated parent melt composition for merrillite (~10–20 × CI) is slightly enriched in heavy REE (HREE), in contrast to the calculated composition for orthopyroxene, which is strongly HREE-depleted. The model assumes mineral/melt partition coefficients (D values) as follows: for orthopyroxene, the median D values of Schwandt and McKay (1996) were assumed, with Gd interpolated; for merrillite, the D values of Joliff et al. (1993) (low REE-concentration case) were assumed. The CI chondrite abundances of Anders and Grevesse (1989) were used for normalization.

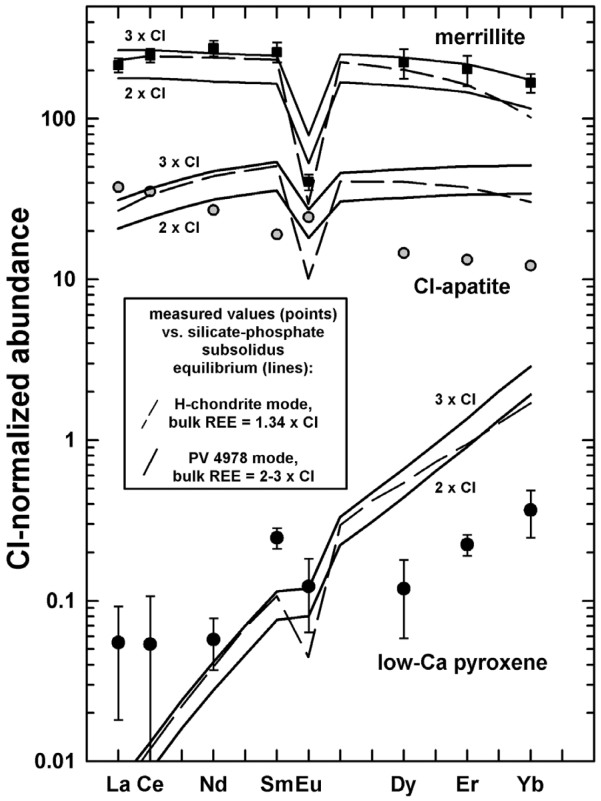

Fig. 14. Measured REE abundances for merrillite, Cl-apatite, and orthopyroxene (points, Table 5) are compared to models in which these phases equilibrated under subsolidus conditions, assuming either a mode identical to that of average PV 4978 (Table 2) with total REE abundances of 2–3 × CI chondrites, or a mode corresponding to average normative H chondrite (Jarosewich 1990) with total REE abundances of 1.34 × CI chondrites (Wasson and Kallemeyn 1988). The models assume partition coefficients identical to those given at magmatic temperatures as follows: orthopyroxene and merrillite—same as in Fig. 13; olivine—McKay (1986), with Eu, Dy, and Er interpolated; clinopyroxene—McKay et al. (1986), Wo_{40} augite, with Dy and Er interpolated, and a Eu anomaly (calculated from Sm/Eu) identical to that of orthopyroxene; plagioclase (all REE except Eu) Drake and Weill (1975), with Yb assumed to be the same as Er; plagioclase (Eu)—Weill and McKay (1975); apatite—Watson and Green (1981). The CI chondrite abundances of Anders and Grevesse (1989) were used for normalization. See text for discussion.

of coarse merrillite and Cl-apatite in Portales Valley. Temperatures were sufficiently high to melt phosphate in PV (see Melting and Crystallization Models for Siderophile Elements section), which may have contributed to the highly non-uniform distribution of phosphate and its often coarse grain size (up to a few mm across), much larger than typical in ordinary chondrites (<<1 mm; Fuchs 1969). Coarse merrillite sometimes shows what appears to be poikilitic textures (Fig. 2b), suggestive of crystallization from melt. Coarse phosphate veins (Fig. 2c) probably formed by crystallization from liquid as they extend trends formed by metal and troilite veins, which were themselves probably molten.

Although phosphate may have melted, it appears that its composition reflects subsolidus equilibration rather than igneous processes. Phosphate in PV has major and trace element compositions typical to that found in equilibrated ordinary chondrites (Fig. 9b; Ruzicka et al. 1999a; Floss et al. 2002), providing no evidence for any unusual chemical processing. Figure 13 shows the REE composition of melt that would be needed to be in equilibrium with merrillite and orthopyroxene, which were analyzed in the same samples. These do not agree, with the merrillite melt pattern showing a flat to HREE-enriched pattern at ~10–20 × CI and the orthopyroxene melt pattern showing a strongly LREE-enriched pattern from ~3–100 × CI (Fig. 13). This discrepancy implies that merrillite and orthopyroxene did not equilibrate with a single melt, even in poikilitic areas. Moreover, partial melting would be expected to produce an LREE-enriched pattern for a melt, but this is opposite to the HREE-enriched pattern shown by merrillite (Fig. 13). Evidently, the composition of merrillite does not reflect equilibration with a partial melt.

Figure 14 compares observed REE abundances in merrillite, apatite, and orthopyroxene with two models in which REE abundances are established by subsolidus equilibration, using the approach of Curtis and Schmitt (1979)

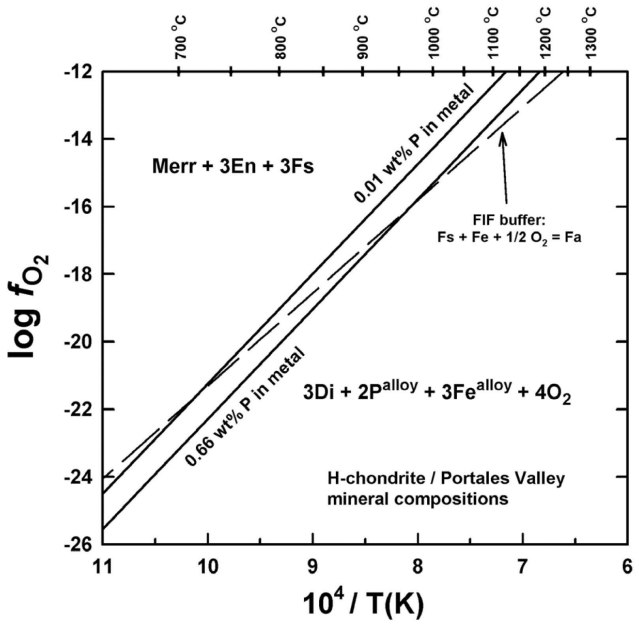

Fig. 15. Temperature-oxygen fugacity conditions for reactions relevant to the petrogenesis of phosphate in Portales Valley. The FIF buffer probably controls fO_2 in ordinary chondrite-like assemblages (McSween and Labotka 1993), whereas merrillite is believed to have formed by the DIMO reaction (given by Reaction 2 in the Text.). The intersection of these equilibria will control the P content in metal and the formation of phosphate. This analysis implies that metal with an initial P content of 0.66 wt% (appropriate to that for PV) will begin to react to form phosphate as temperature drops below ~975 °C. Reaction will continue until a temperature of ~725 °C is reached, which corresponds to the observed P content in metal.

and Treiman (1996). Both models assume silicate-phosphate equilibrium between the chief non-metallic minerals found in H chondrites and PV (merrillite, apatite, plagioclase, clinopyroxene, orthopyroxene, and olivine), and both assume that relative D values for these phases at subsolidus conditions are identical to those found at magmatic temperatures. The models differ in that an H chondrite mode and bulk REE abundance (about 1.3 × CI) is assumed in one case, whereas a mode appropriate to that in PV 4978 and a bulk REE abundance of 2–3 × CI is assumed for the other case.

Both of the subsolidus equilibration models shown in Fig. 14 roughly agree with the overall REE abundances found in merrillite, apatite, and orthopyroxene, but both fail to precisely account for the observed phase compositions, especially for Cl-apatite and orthopyroxene. For example, the predicted Cl-apatite patterns show negative Eu anomalies and HREE-enriched patterns, whereas the observed pattern is opposite of this. The predicted HREE/LREE ratio for orthopyroxene is also much steeper than observed. Finally, the calculated patterns for merrillite resemble the observed composition except for having too much Yb (for an H chondrite mode) or too much Eu (for a PV4978 mode) (Fig. 14). These results are interpreted to indicate that there was an approach to subsolidus REE equilibrium in PV, but that equilibrium was not fully maintained, or that the assumed D values are not exactly appropriate.

The close spatial association of phosphate with coarse metal suggests a genetic relationship between these phases. Most likely, phosphate formed by reaction of a P-bearing metal component with a Ca-bearing pyroxene component, in either the solid or liquid states. This type of redox reaction is proposed to have occurred to form phosphate minerals in stony, stony-iron, and iron meteorites (Olsen and Fuchs 1967; Murrell and Burnett 1983; Harlow et al. 1984). Reaction between metal and silicate can explain why phosphate is concentrated at the metal-silicate contact in PV, if phosphate formation was limited by the availability of P in metal. In addition, formation of phosphate by reaction between Ca-pyroxene in the silicate fraction and P-bearing metal is consistent with the modal mineralogy of PV 4978, which is depleted in clinopyroxene compared to average H chondrites (see Modal Composition section).

A phosphate-forming redox reaction of the following type is implied for Portales Valley:

$$\underset{\text{diopside}}{CaMgSi_2O_6} + \underset{\text{metal}}{2P} + \underset{\text{metal}}{3Fe} + \underset{\text{gas}}{4O_2}$$

$$\Rightarrow \underset{\text{merrillite}}{Ca_3(PO_4)_2} + \underset{\text{orthopyroxene}}{3MgSiO_3} + \underset{\text{orthopyroxene}}{3FeSiO_3} \qquad (2)$$

In Reaction 2 (abbreviated DIMO, where *D* = diopside, *I* = iron, etc.), P in metal is oxidized and Ca-pyroxene is removed. Oxygen fugacity in PV may have been controlled by internal buffering between Fe-bearing olivine, orthopyroxene, and metal according to the reaction:

$$\underset{\text{ferrosilite}}{FeSiO_3} + \underset{\text{metal}}{Fe} + \underset{\text{gas}}{\frac{1}{2}O_2} = \underset{\text{fayalite}}{Fe_2SiO_4} \qquad (3)$$

Reaction 3 (FIF) has been proposed to be the principal oxygen buffer in ordinary chondrites (McSween and Labotka 1993).

The temperature-oxygen fugacity conditions of the DIMO Reaction 2 were evaluated with a thermodynamic model assuming phase compositions for olivine, low-Ca pyroxene, high-Ca pyroxene, and metal appropriate to those in Portales Valley and H chondrites (Tables 3 and 4). This model is essentially equivalent to that derived by Harlow et al. (1984) for mesosiderites (their Reaction T, model 2), except that different phase compositions were used. The thermodynamic parameters assumed were: ideal mixing of Fe in Fe-Ni taenite (Fraser and Rammensee 1982) with $X_{Fe} = 0.902$; regular solution model for Fe-Mg olivine (Williams 1971) with $X_{Fa} = 0.18$; regular solution model for Mg-Ca clinopyroxene (Holland et al. 1979) with $X_{Di} = 0.823$; regular solution model for Fe-Mg orthopyroxene (Williams

1971) with $X_{Fs} = 0.18$; and pure $Ca_3(PO_4)_2$ merrillite. For P in metal, an activity coefficient of $\gamma_P = 1.17 \times 10^{-5}$ was assumed, which is consistent with the data of Komarek (1963) at 1050 °C, and which is able to reproduce the experimentally-determined metal-silicate-phosphate equilibria of Friel and Goldstein (1976) for metal with 0.167 wt% P. Thermodynamic data for the FIF equilibrium were taken from Williams (1971) (his OPI reaction).

Figure 15 shows equilibrium T-fO_2 conditions for the DIMO and FIF reactions. Equilibria for two different P contents in metal (0.66 and 0.01 wt%) are shown for the DIMO reaction. The 0.01 wt% P line corresponds to the amount of P currently observed in Portales Valley metal, whereas the 0.66 wt% line corresponds to the amount of P that could have been present in PV metal initially if all P is put back into metal. The 0.66 wt% P value was calculated by combining the average P content in AMNH 4978 (Table 6) with the average amount of metal in this sample (Table 2). Figure 15 is split into two regions to indicate that diopside + P-rich metal form a stable assemblage at high temperature and that merrillite + orthopyroxene form a stable assemblage at low temperature.

If solid metal was present and the FIF buffer (Reaction 3) controlled fO_2, the equilibrium temperature-fO_2 range of the phosphate-forming reaction in PV would be constrained by where the FIF equilibrium (Reaction 3) (dashed line in Fig. 15) intersects the DIMO equilibrium (Reaction 2) for a given P content in metal (solid lines in Fig. 15). For about 0.66 wt% P in metal initially, reaction to form phosphate would occur at temperatures as high as ~975 °C (Fig. 15). For 0.01 wt% P in metal, phosphate would be formed at temperatures as high as ~725 °C. This indicates that upon cooling from the high temperatures reached in PV (see Melting and Crystallization Models for Siderophile Elements section) and for the P contents inferred, solid metal would react with clinopyroxene to produce phosphate starting at ~975 °C and continue until the temperature reached ~725 °C, at which point diffusion could have became too slow to maintain equilibrium.

For a metal P content of 0.66 wt%, this upper temperature limit for producing merrillite (~975 °C) is close to but slightly below the Fe-S eutectic temperature of ~990 °C and above the Fe-Ni-S eutectic temperature of ~940 °C. This suggests that much of the phosphate in PV formed by reaction under metamorphic conditions, after metal, sulfide, and silicates had crystallized. However, at the highest temperatures reached in PV, phosphate was probably at least partly melted and P would have resided in liquid that was interacting with metal. Some phosphate may have crystallized directly from liquid, resulting in phosphate veins and poikilitic phosphate.

The analysis presented above is consistent with the lack of coarse schreibersite in Portales Valley. Figure 16 compares composition-temperature relationships for metal-phosphide equilibria (Moren and Goldstein 1979) with the metal-silicate-phosphate equilibria described above and shows the likely evolution of P content in PV metal with an initial P content of ~0.6 wt% and a final P content of ~0.01 wt%. Figure 16 suggests that merrillite would form instead of schreibersite as temperature decreased. Once phosphate started to form, it would control the P content in metal until the currently observed low P content was attained and the closure temperature for the DIMO reaction was reached. Schreibersite would not form before phosphate unless the P content in metal was locally higher than ~1 wt%. Even if the P content was this high, schreibersite would react to form phosphate as temperature decreased. For instance, taenite cooling from high temperature under P-rich (>1 wt%) conditions would follow the taenite-shreibersite (GUP) equilibrium (Fig. 16). When the temperature dropped to ~975 °C, merrillite would form as before and schreibersite would become unstable. In either case, schreibersite would not be stable as temperature fell. This scenario is consistent with the lack of coarse schreibersite in PV, but we have observed rhabdites in PV coarse metal. Such rhabdites probably formed by exsolution from metal (Doan and Goldstein 1969) at a temperature below the apparent closure temperature of ~725 °C for the DIMO reaction.

As was the case for producing large graphite nodules (see Origin of Large Graphite Nodules section), the presence and distribution of coarse phosphate in Portales Valley can be attributed ultimately to initially high temperatures and a high concentration of a critical component (in this case, P) in the metallic phase. Metal that was mobilized at high temperatures was evidently able to scavenge P from large regions of the meteorite and concentrate it into a smaller volume of metal. As the assemblage cooled, buffering reactions favored the production of phosphate at the expense of P-bearing metal and schreibersite and P became localized in coarse phosphate adjacent to metal.

Olivine/Pyroxene Ratio

Besides the redox reactions that formed phosphate and removed clinopyroxene (see Petrogenesis of Coarse Phosphate: Igneous or Metamorphic? section), redox reactions can also explain the low olivine/pyroxene ratio observed in metal-rich samples of PV compared to H chondrites (Fig. 5). Reduction of iron in Fe-olivine would occur if Reaction 3 were operative and if it proceeded to the left. This can be rationalized, as the phosphate-forming DIMO Reaction 2 would necessarily consume O_2, and this would tend to drive Reaction 3 to the left, in the direction of increased Fe-orthopyroxene and diminished Fe-olivine. An additional reaction involving breakdown of Mg-olivine to Mg-orthopyroxene would be needed to prevent Fe/Mg ratios in mafic silicates from changing, as required if equilibrium was maintained. This process would consume olivine and produce orthopyroxene, lowering the olivine/pyroxene ratio.

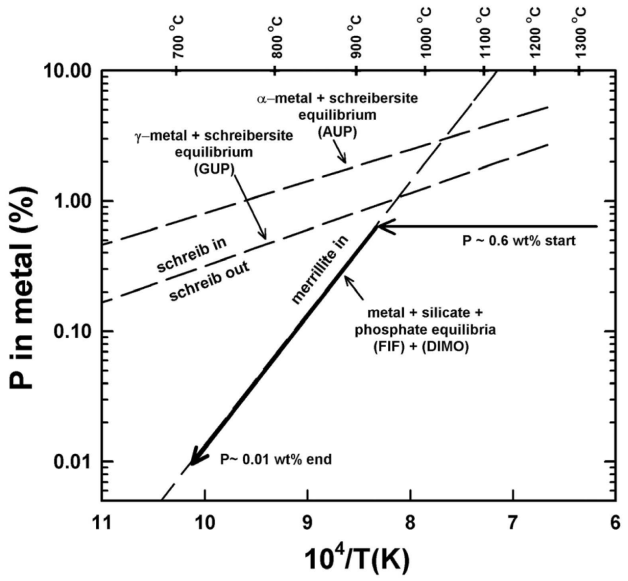

Fig. 16. Modelled evolution of P content in the metal of Portales Valley as a function of temperature. In principle, the P content in metal under subsolidus conditions could be controlled either by metal-silicate-phosphate (FIF and DIMO) equilibria or metal-phosphide equilibria (GUP or AUP), but our analysis suggests that for the range of P contents likely present in PV metal (P ≤ 0.6 wt%), equilibria with silicates and the formation of phosphate likely controlled the evolution of P content in metal.

Subsolidus Thermal History

Portales Valley appears to have experienced protracted subsolidus annealing. Evidence for this includes the formation of phosphate and removal of clinopyroxene to temperatures as low as ~725 °C, as implied by the P content in metal (see Petrogenesis of Coarse Phosphate: Igneous or Metamorphic? section); metallographic data that indicates slow cooling at low temperatures; and pyroxene geothermometry.

All researchers agree that PV cooled slowly under subsolidus conditions to produce Widmanstätten textures, Fe-Ni zoning in metal, and the microtextures of metal (Ruzicka et al. 1999b: Kring et al. 1999b; Pinault et al. 1999; Rubin and Ulff-Møller 1999; Haack et al. 2000; Rubin et al. 2001; Sepp et al. 2001). Different metallographic approaches yield cooling rate estimates that converge on a value of about a few °C/Ma. These include minimum Ni contents at kamacite-taenite interfaces (Ruzicka et al. 1999: ~0.5–7 °C/Ma), central Ni contents in taenite (Pinault et al. 1999: ~5 °C/Ma), Ni profile matching (Haack et al. 2000: ~2 °C/Ma), and microstructures in the cloudy zone of taenite, both in coarse and fine metal (Sepp et al. 2001: 6.5 ± 2.1 °C/Ma). These cooling rates are pertinent at the low temperatures (~350–700 °C) implied by the Fe-Ni phase diagram (e.g., Kubaschewski 1982; Reisener and Goldstein 2003) for PV-like metal compositions. Although slow, these cooling rates are not unusually slow compared to those inferred for chondrites and iron meteorites based on metallographic methods (Ruzicka et al. 1999b).

Two-pyroxene geothermometry for PV is also consistent with relatively slow rates of cooling at a somewhat higher temperature. High-quality analyses of low-Ca pyroxene and augite were used to estimate pyroxene equilibration temperatures based on a graphical pyroxene geothermometer (Lindsley and Andersen 1983; Lindsley 1983). With this geothermometer, temperature estimates to a precision of roughly ±10 °C can be made. For low-Ca pyroxene (N = 40 analyses), the estimated temperature is 770 ± 60 °C (mean and standard deviation, respectively), with individual values ranging between 900–650 °C. For augite (N = 13), the calculated temperature is 900 ± 35 °C, ranging between 995–870 °C. For comparison, McSween and Patchen (1989) used the same geothermometer and found temperatures for type 6 ordinary chondrites of ~800–900 °C for orthopyroxene and ~900–960 °C for clinopyroxene. The values for Portales Valley overlap those in type 6 ordinary chondrites, but are somewhat lower.

If one interprets these temperatures as closure temperatures that should decrease as cooling rate decreases, PV cooled somewhat more slowly than a typical H chondrite at temperatures of about 700–950 °C. The difference in derived temperatures for PV orthopyroxene and augite (~130 °C on average) imply that these pyroxenes were not in complete equilibrium at these temperatures, probably owing to sluggish diffusion. Kinetic barriers to diffusion also appear to have prevented PV metal from losing even the small amount of P (0.01 wt%) it still contains (Reisener and Goldstein 2003).

Slow subsolidus cooling implies that Portales Valley cooled at depth within its parent body (e.g., Kring et al. 1999a, 1999b). However, PV does not appear to have cooled any more slowly than other ordinary chondrites at low temperatures (about 350–700 °C) and only slightly more slowly than typical type 6 chondrites at somewhat higher temperatures (about 700–950 °C). The main differences between PV and H6 chondrites arose because temperatures were higher in PV (about 940–1150 °C) (see Melting and Crystallization Models for Siderophile Elements section). These higher temperatures were probably sustained for a relatively long period, with sufficient time for metal to migrate throughout the breccia and silicate clasts to float (see Textural Evidence for Melting of Metal section). The thermal history we infer for the meteorite is appropriate to a deep parent body setting, which enabled slow cooling to temperatures <500 °C.

Origin of Metal Veins

It is apparent that the inhomogeneous distribution of metal in PV reflects the removal of metal from large portions

of the Portales Valley breccia and its concentration into larger sheet-like structures (veins) (Kring et al. 1999b; Pinault et al. 1999a; Rubin et al. 2001). This implies that much of the metal in PV was mobile, either because it was able to flow in a ductile fashion or because it was liquefied (or some combination of both). Mobilization as a fluid is not hard to imagine. However, the models discussed above (see Melting and Crystallization Models for Siderophile Elements section) suggest that the overall compositional and textural features of metal in PV were established with most of the metallic fraction being solid. Unless temperatures were higher than inferred, it seems inescapable that metal would have had to flow into veins partly in a solid state. Solid-state flow would have to occur through what were likely constricted passageways in silicates.

It is unclear why metal would have been concentrated into coarse vein-like structures, but a role for hypervelocity impact seems likely. Partial melting experiments of chondrites and chondrite analogues under static conditions show that metallic melts tend to form isolated patches or globules, not veins, with little tendency for metallic melts to separate from silicate (Takahashi 1983; Jurewicz et al. 1995; Rushmer et al. 2000b; Feldstein et al. 2001). Vein-like intergrowths of metal and sulfide have been reported in heating experiments of chondrites after a one week heating at 700–1000 °C (McSween et al. 1978) and after a one hour heating at 1200 °C (Feldstein et al. 2001), but such veins tend to be small (~1–2 μm wide, rarely up to 100–150 μm long) and do not approach either the coarseness or connectivity of veins in PV. In addition, veins do not persist in longer duration heating episodes at 1200 °C (Feldstein et al. 2001), suggesting that metal vein formation is not a prevalent feature of static melting. Metal may have filled cracks that were produced by impact brecciation prior to heating (Pinault et al. 1999; Scott and Pinault 1999), but coarse veins are not produced by heating natural chondrite samples that have been weakly shocked and fractured (McSween et al. 1978; Feldstein et al. 2001). Alternatively, metal may have been melted and concentrated into narrow zones by a hypervelocity impact (e.g., Kring et al. 1999b; Rubin et al. 2001). However, although FeNi metal veins up to 1 mm wide are present in shocked chondrites (Rubin 1985), the shock stage of PV is low (see Shock Stage and Deformation section) and metallic veins as coarse as in PV have not been described in other chondrites (Rubin 1985), whether shocked or not (Pinault et al. 1999).

A combination of elevated temperatures and a relatively weak shock event could have produced the Portales Valley vein and breccia texture. Experiments have shown that metal and troilite can be mobilized into small-scale (a few μm wide) metal and troilite veins by shear deformation with strain rates of 10^3 to 10^4 s^{-1} at ambient room pressures and temperatures (Van de Bogart et al. 2003). Such shearing can occur without entailing an increase in shock stage (Van de Bogart et al. 2003). Experiments involving heating under conditions of differential stress indicate that metal and sulfide can be mobilized into larger interconnected veins that surround silicate clasts (Rushmer et al. 2000a, 2000b). For example, experiments performed on the Kernouvé H6 chondrite with a strain rate of 10^{-5} s^{-1} at 925–990 °C and a confining pressure of 1 GPa produced cataclastic metal-silicate zones up to 100 μm wide, with metal enclosing silicate clasts (Rushmer et al. 2000a). The texture produced in these experiments is similar to, albeit still not as coarse as, that in Portales Valley. Moreover, the composition of mobilized (solid + liquid) metal in these experiments (Rushmer et al. 2004) show some similarities to the metal in PV. This suggests that the veins in PV could have formed by shear-induced mobilization of metal and sulfide at elevated temperature. In these shearing experiments, it appears that strain rates may be less critical than ambient temperature in producing coarse veins.

Even if static heating or impact were able to produce coarse veins of the sort found in Portales Valley, it is unclear why a solid metal (as opposed to liquid metal) component became concentrated there. Based on the models described earlier, it appears that taenite parent crystals grew preferentially inside larger metallic vein bodies and expelled metallic liquid into surrounding silicate-rich areas as they grew. Continuity of Widmanstätten structures across large veins implies that entire veins consist of single parent taenite crystals, suggesting either that the growth rate of taenite in veins was high relative to the number of nucleation sites or that taenite grains in coarse veins were recrystallized into large grains before cooling to low temperatures. Preferential growth of taenite in veins could possibly have been caused by a nucleation or surface energy effect, with large silicate-free, taenite-bearing melt zones serving as favorable sites for additional growth of taenite. If the interfacial energy between solid metal and solid silicate were high compared to that between liquid metal and solid silicate, this could have caused solid metal to migrate to silicate-poor areas and S-rich metallic melt to become concentrated in silicate-rich areas, as observed in PV. Preferential growth of taenite on pre-existing taenite grains in the silicate-poor areas would have produced the coarse grains in the veins.

Preferred Model for Forming Portales Valley

The two leading models for the origin of Portales Valley envisage important roles for impact melting (Kring et al. 1999b; Rubin et al. 2001) or internal parent body heating (Pinault et al. 1999; Scott and Pinault 1999). In the first case, PV could be a variant of an impact-melt breccia; in the second, it could be analogous to primitive achondrites such as acapulcoites or winonaites.

Our preferred model is a blend of these two extremes. On balance, evidence favors impact-triggered fluidization of

metal that is already warm as the best explanation of the overall cataclastic and metal-veined texture of Portales Valley. We agree with some researchers that impact heating alone is unlikely to be viable for explaining Portales Valley (Kring et al. 1999b; Pinault et al. 1999; Scott and Pinault 1999; Haack et al. 2000), owing to the large collisional velocity that would be needed, which would probably result in parent body disruption and fast cooling at high temperatures (Haack et al. 2000). By the same token, we agree with other researchers (Kring et al. 1999b; Rubin et al. 2001) that the coarse veins in PV were most likely produced by shock (see Origin of Metal Veins section). The elevated abundance of gallium in the coarse vein metal (see Bulk Composition section) is consistent with redistribution of this element during shock-heating (Chou and Cohen 1973). We speculate that a shock event involving shear could have mobilized metal even under S1 shock stage conditions (≤4–5 GPa; Stöffler et al. 1991), when temperatures were relatively high (~900–950 °C, typical for that of type 6 chondrites; McSween and Patchen 1989) at the time of impact. Following impact-triggered fluidization to form veins, the meteorite experienced high temperatures and slow cooling from supersolidus to subsolidus temperatures, which enabled metal to separate from troilite, graphite to crystallize in large nodules, redox reactions to proceed in large portions of the meteorite, phosphate to crystallize and metamorphically grow in large grains, and Widmanstätten texture to form in metal. This protracted heating implies that PV cooled at depth within a parent body which remained intact. Portales Valley could have originated below a large impact crater on the parent body, as first suggested by Kring et al. (1999a, 1999b). Alternatively, Portales Valley could have formed by the accretion of planetesimals that were already hot, involving low collisional velocities (Haack et al. 2000).

Although a role for shock is indicated as a trigger for metal-sulfide mobilization and the formation of cataclastic textures, we do not find compelling evidence that this shock involved high pressures. Non-traditional shock indicators present in PV, such as small amounts of metallic Cu and rare plagioclase-chromite intergrowths (Rubin 1993, 2003, 2004) have not been calibrated for peak pressures and consequently do not place tight constraints on shock levels. The shock-blackening found locally in Portales Valley (Rubin et al. 2001; Kring et al. 1999b) is often associated with shocked meteorites, but can be produced by a shearing action without resulting in an increase in shock stage (Van de Bogart et al. 2003). Our XRD and Raman data for PV graphite are consistent with a modest shock event involving shock pressures of ~5–10 GPa, with the shock probably being closer to the lower value (see Shock Stage and Deformation section). Although a shock stage as high as S3 (~15–20 GPa maximum; Stöffler et al. 1991; Bischoff and Stöffler 1992) followed by annealing of shock features has been proposed for PV (Kring et al. 1999a,b; Rubin et al. 2001), our data do not require this. We find no evidence to support the idea that PV was initially shocked to a shock stage as high as S6 (Rubin 2004).

In our model, most of the heat necessary for mobilizing and melting metal and sulfide was provided by internal heat in the parent body, before the relatively weak shock event that triggered the formation of veins. We thus assign an important role to internal heating in the formation of Portales Valley, in agreement with the model of Pinault et al. (1999) and Scott and Pinault (1999). The temperatures implied for Portales Valley at the time solid and liquid metal last equilibrated are about 940–1150 °C, which suggests a post-shock temperature increase of about 0–250 °C when compared to a typical H6 chondrite heated to about 900–950 °C. The modest post-shock temperature increase would correspond to shock pressures of about 0–30 GPa, or shock stages S1-S4, based on experiments performed at room temperature (Stöffler et al. 1991). To produce the current S1 shock stage from S4, significant recovery of shock defects in PV would have had to occur. However, as noted above, our data are consistent with the possibility that PV was affected by a shock event too weak (shock stage S1 or S2) to result in many shock defects, with only modest post-shock recovery needed. Additional microstructural (i.e., TEM) data might help discriminate between these possibilities.

Are Chronologic Data Consistent with the Preferred Model?

According to our preferred model, Portales Valley formed as a result of a shock event that affected a target that was already warm. This most likely requires that the veining and cataclasis event that affected PV was established early in the solar system, when internal heating mechanisms for asteroids, such as short-lived radionuclide decay or electromagnetic induction heating, were active. If late impact events were responsible for breccia, vein, and phosphate formation, our preferred model for forming PV in the early solar system would be invalidated.

Age data involving a variety of chronometers have been obtained for Portales Valley (Chen et al. 1999, 2000; Garrison and Bogard 2001; Papanastassiou et al. 2001, 2002) that can test whether our preferred model is viable. Evidence for early formation (about 4.4–4.6 Ga) consistent with our model is provided by U-Th-Pb, ^{39}Ar-^{40}Ar, and Rb-Sr data for bulk silicate-rich material, and by Re-Os data for coarse metal. Later disturbances are suggested by an absence of short-lived radionuclide decay products, a secondary U-Th-Pb age of 94 Ma, scatter in Rb-Sr ages, apparently late Re/Os fractionation in fine-grained metal, and young T_{CHUR} Sm-Nd ages of 1.16–1.85 Ga.

We suggest that Re/Os variation in fine-grained metal might not represent a datable late event, but that it is related

to the melting event that produced veins. We have shown that compared to H chondrites, fine-grained metal is more fractionated than the coarse vein metal, consistent with the results of Chen et al. (1999, 2000), and that variations in siderophile element compositions for metal in Portales Valley probably reflect various proportions of solid and liquid metal components (see Melting and Crystallization Models for Siderophile Elements section). This leads us to suspect that the differences in apparent Re-Os ages for fine- and coarse-grained metal (Chen et al. 1999, 2000) reflect sampling different amounts of solid and liquid metal components, and that the apparently younger ages for the fine metal may represent the effects of mixing, rather than a true age.

Although various explanations have been advanced to explain the young Sm-Nd T_{CHUR} ages for Portales Valley (Papanastassiou et al. 2002; Ruzicka and Killgore 2002; Floss et al. 2002), our favored explanation is that they, too, represent mixing effects and not ages. One reason to infer a mixing effect is the variation in Sm and Nd abundances and Sm/Nd that would result from sampling differing amounts of phosphate and clinopyroxene in bulk samples of Portales Valley (see Chemical Fractionations and Mixing Models section). Moreover, the Sm-Nd T_{CHUR} ages are suspect as they scatter considerably. We used the data given in Papanastassiou et al. (2002) to plot a standard Sm-Nd isochron diagram to see whether a well-defined isochron could be obtained. We found a correlation line indicative of an apparent age of about 1.54 Ga (using a decay constant for ^{147}Sm of 6.54×10^{-12} a^{-1}), with considerable scatter ($R^2 = 0.9487$) for this correlation. This apparent young age is consistent with the reported T_{CHUR} ages, but the large scatter suggests it may not have chronologic significance.

Altogether, our interpretation of the chronologic data that have been obtained for Portales Valley suggest that an early formation age is likely, consistent with our preferred model. Complexities in the bulk Re-Os and Sm-Nd systems which could be interpreted as evidence for younger ages can instead be plausibly interpreted as resulting from mixing effects.

Classification of Portales Valley and Relationship to Other Meteorite Classes

Portales Valley is currently classified as an H6 chondrite (Grossman 1999) with a shock stage listed as S3 (Koblitz 2003). Subsequently, additional data have been obtained for the meteorite indicating that this classification is misleading. As we demonstrated, the most accurate shock designation for PV is S1, or at most S2. Moreover, although the mineral chemistry of silicates and phosphates is appropriate to an H chondrite, the major and trace element composition of metal is somewhat anomalous, large portions of the meteorite do not have an H chondrite mineralogy or bulk composition, no other ordinary chondrite contains coarse metal veins, and no other ordinary chondrite has been found with large graphite nodules. The presence in PV of coarse merrillite that locally forms poikilitic grains and veins is also exceptional. Even in most hand-specimens, there is no mistaking Portales Valley for a typical H6 chondrite.

Based on our work, it seems clear that the metal-sulfide and even the silicate portion of the meteorite was partly melted, suggesting that the petrographic grade of Portales Valley is higher than six. Considering this likely partial melt origin for PV, the H chondrite-like mineral compositions for most phases, and our inference of a mainly endogenic heat source (see Preferred Model for Forming Portales Valley section), Portales Valley can be properly regarded as a primitive achondrite related to H chondrites. In other words, it is an H7 achondrite. As there is clear evidence for fluidization and partial melting of metal as well as for brecciation and cataclasis, we also conclude that PV is the first well-documented example of a metallic-melt breccia. Future work may reveal other meteorites that have coarse metallic-melt veins or a similar inferred history. In this event, Portales Valley and such meteorites could be classified as "Portalesites," with Portales Valley as the type example. Given that only one example of this potential new class of meteorites is now recognized, it may be premature to assign this group name to PV. In the meantime, we suggest that Portales Valley is more accurately classified as an H7 (S1) metallic-melt breccia.

The main importance of Portales Valley may ultimately lie in what the meteorite has to tell us about the formation of other meteorite classes. Clearly, the silicate protolith of PV was an H chondrite. It is also clear that PV was partly melted, possibly analogous to the melting processes that affected achondrites and iron meteorites. Previous workers have noted that the textures of silicates and the distribution of metal and sulfide in PV are similar to those in acapulcoites, winonaites, and silicated IAB irons (Scott and Pinault 1999; Pinault et al. 1999) and that Portales Valley has chemical-isotopic-textural links to silicated IIE irons (Scott and Pinault 1999; Ruzicka et al. 1999a; Ruzicka et al. 2000a; Rubin and Ulff-Møller 1999). Indeed, the vein-and-breccia texture of Portales Valley is remarkably similar to the silicated IIE iron meteorite Netschäevo (Ruzicka et al. 1999a; Rubin et al. 2001) and to IAB iron meteorites that contain angular or subangular silicate clasts, such as Leuders (McCoy et al. 1996) and some samples of Campo del Cielo (Benedix et al. 2000).

Thus, the processes that formed Portales Valley may have also operated to produce other achondrites and iron meteorites, especially primitive achondrites and silicated iron meteorites. More work is needed to establish the extent to which the overall origin inferred for PV—partial melting caused by simultaneous endogenic heating and impact-induced mobilization of metal—can be applied to these other differentiated meteorites.

CONCLUSIONS

Our data suggest that the PV meteorite is a well-documented example of a metallic-melt breccia. The meteorite probably formed as a result of a shock-triggered event during internal heating of the parent body early in the history of the solar system, forming and cooling at depth within its parent body. The composition of metal in PV is somewhat anomalous and best explained by a model involving equilibrium partial melting and incomplete separation of solid and liquid metal at temperatures not far above the metal-sulfide eutectic (~940–1150 °C). Under these conditions, most C and P were probably incorporated into metallic liquid. Graphite nodules probably formed by crystallization from this metallic liquid and phosphate formed by reaction between P-bearing metal and clinopyroxene components. Trace element and major element abundances in phosphate were largely established under subsolidus conditions and reflect an approach to equilibrium by buffering reactions in the H-chondrite-like mineral assemblage as it cooled between ~975–725 °C. Phosphate-forming and FeO-reduction reactions were widespread in PV and entailed a change in the mineralogy of the stony portion. Portales Valley is best classified as an H7 (S1) metallic-melt breccia and can be considered to be a primitive achondrite, but one in which shock played a crucial role. Various textural, mineralogic, chemical, and isotopic features of PV are reminiscent to those in silicated iron meteorites. Thus, Portales Valley is somewhat transitional between more primitive (chondritic) and evolved (achondrite, iron) meteorite types, and could be providing clues as to how differentiation in some asteroidal bodies occurred.

Acknowledgments–The authors wish to thank Dr. Georg Grathoff for his assistance and for the use of X-ray diffraction equipment at Portland State University, Allan Patchen and Dr. Roger Nielsen for their assistance in operating electron microprobes at the University of Tennessee and Oregon State University, respectively, Joe Boesenberg for discussion regarding Portales Valley samples at the American Museum of Natural History, Dr. Tracy Rushmer for sharing images of experimental run products, Dr. John McHone for helping to arrange Raman spectroscopy studies of the graphite nodule, Dr. Hiroko Nagahara for editorial handling, constructive reviews by Dr. Henning Haack and an anonymous reviewer, and an informal review by Dr. Melinda Hutson. The first author also wishes to thank the late Dr. Martin Prinz for stimulating an interest in research on PV. This work was supported in part by NASA grant NAG5-12856 (A. Ruzicka).

Editorial Handling—Dr. Hiroko Nagahara

REFERENCES

Affiatalab F. and Wasson J. T. 1980. Composition of the metal phases in ordinary chondrites: Implications regarding classification and metamorphism. *Geochimica et Cosmochimica Acta* 44:431–446.

Allen R. O. and Mason B. 1973. Minor and trace elements in some meteoritic minerals. *Geochimica et Cosmochimica Acta* 37: 1435–1456.

Anders E. and Grevesse N. 1989. Abundances of the elements: Meteoritic and solar. *Geochimica et Cosmochimica Acta* 53:197–214.

Benedix G. K., McCoy T. J., Keil K., and Love S. G. 2000. A petrologic study of the IAB iron meteorites: Constraints on the formation of the IAB-Winonaite parent body. *Meteoritics & Planetary Science* 35:1127–1141.

Brearley A. and Jones R. H. 1998. Chondritic meteorites. In *Planetary materials*, edited by Papike J. J. Washington, D. C.: Mineralogical Society of America. pp. 3-1–3-398.

Britt D. T. and Kring D. A. 2001. Portales Valley: The bidirectional spectrum of a unique H5 breccia (abstract #1475). 32nd Lunar and Planetary Science Conference. CD-ROM.

Bischoff A. and Stöffler D. 1992. Shock metamorphism as a fundamental process in the evolution of planetary bodies: Information from meteorites. *European Journal of Mineralogy* 4: 707–755.

Chabot N. L. and Jones J. H. 2003. The parametrization of solid metal-liquid metal partitioning of siderophile elements. *Meteoritics & Planetary Science* 38:1425–1436.

Chen J. H., Papanastassiou D. A., and Wasserburg G. J. 1999. Re-Os and Pd-Ag systematics in the metal-rich chondrite Portales Valley (abstract #1472). 30th Lunar and Planetary Science Conference. CD-ROM.

Chen J. H., Papanastassiou D. A., and Wasserburg G. J. 2000. Comparative FeNi and silicate chronology in Portales Valley (abstract #1507). 31st Lunar and Planetary Science Conference. CD-ROM.

Chou C.-L. and Cohen A. J. 1973. Gallium and germanium in the metal and silicates of L and LL chondrites. *Geochimica et Cosmochimica Acta* 37:315–327.

Chou C.-L., Baedecker A. A., and Wasson J. T. 1973. Distribution of Ni, Ga, Ge, and Ir between metal and silicate portions of H group chondrites. *Geochimica et Cosmochimica Acta* 37:2159–2171.

Crozaz G., Pellas P., Bourot-Denise M., de Chazal S. M., Fiéne C., Lundberg L. L., and Zinner E. 1989. Plutonium, uranium and rare earths in the phosphates of ordinary chondrites—The quest for a chronometer. *Earth and Planetary Science Letters* 93:157–169.

Curtis D. B. and Schmitt R. A. 1979. The petrogenesis of L-6 chondrites: Insights from the chemistry of minerals. *Geochimica et Cosmochimica Acta* 43:1091–1103.

Doan A. S. and Goldstein J. I. 1969. The formation of phosphides in iron meteorites. In *Meteorite research*, edited by Millman P. M. Dordrecht, Holland: D. Reidel. pp. 763–779.

Drake M. J. and Weill D. F. 1975. Partition of Sr, Ba, Ca, Y, Eu^{2+}, Eu^{3+}, and other REE between plagioclase feldspar and magmatic liquid: An experimental study. *Geochimica et Cosmochimica Acta* 39:689–712.

Ebihara M., Ikeda Y., and Prinz M. 1997. Petrology and chemistry of the Miles IIE iron. II: Chemical characteristics of the Miles silicate inclusions. *Antarctic Meteorite Research* 10:373–388.

El Goresy A., Gillet P., Mostefaoui S., Chen M., and Masaitas V. L. 2002. A transparent, very hard, dense and unusually disordered form of carbon in heavily shocked gneisses from Popigai, Russia: Petrographic settings and comparison with a similar phase in shocked gneisses from the Ries (abstract #1031). 33rd Lunar and Planetary Science Conference. CD-ROM.

Feldstein S. N, Jones R. H., and Papike J. J. 2001. Disequilibrium partial melting experiments on the Leedey L6 chondrite: Textural controls on melting processes. *Meteoritics & Planetary Science* 36:1421–1441.

Friel J. J. and Goldstein J. I. 1976. An experimental study of

phosphate reduction and phosphorus-bearing lunar metal particles. 7th Lunar Science Conference. pp. 791–806.

Floss C., Crozaz G., Liu M., and Scott E. R. D. 2002. Piecing together the Portales Valley chronology puzzle: Clues to the origin of unusually young Sm-Nd ages (abstract #1084). 33rd Lunar and Planetary Science Conference. CD-ROM.

Fraser D. G. and Rammensee W. 1982. Activity measurements by Knudsen cell mass spectrometry—The system Fe-Co-Ni and implications for condensation processes in the solar nebula. *Geochimica et Cosmochimica Acta* 46:549–556.

Fuchs L. H. 1969. The phosphate mineralogy of meteorites. In *Meteorite research*, edited by Millman P. M. Dordrecht, Holland: D. Reidel. pp. 683–695.

Gaines R. V., Skinner H. C. W., Foord E. E., Mason B., Rosenzweig A., King V. T., and Dowty E. 1997. *Dana's new mineralogy*. New York: John Wiley and Sons.

Garrison D. H. and Bogard D. D. 2001. ^{39}Ar-^{40}Ar and space exposure ages of the unique Portales Valley H chondrite (abstract #1137). 32nd Lunar and Planetary Science Conference. CD-ROM.

Gastineau-Lyons H. K., McSween H. Y., Jr., and Gaffey M. J. 2002. A critical evaluation of oxidation versus reduction during metamorphism of L and LL group chondrites, and implications for asteroid spectroscopy. *Meteoritics & Planetary Science* 37: 75–89.

Grossman J. N. 1999. The Meteoritical Bulletin no. 83. *Meteoritics & Planetary Science* 34:A169–A186.

Haack H., Pedersen T. P., and Rasmussen K. L. 2000. Portales Valley: Thermal history of a unique meteorite (abstract). *Meteoritics & Planetary Science* 35:A67–A68.

Hansen M. and Anderko K. 1958. Constitution of binary alloys. New York: McGraw-Hill.

Harlow G. E., Delaney J. S., Nehru C. E., and Prinz M. 1984. Metamorphic reactions in mesosiderites: Origin of abundant phosphate and silica. *Geochimica et Cosmochimica Acta* 46: 339–348.

Holland T. J. B., Navrotsky A., and Newton R. C. 1979. Thermodynamic parameters of $CaMgSi_2O_6$-$Mg_2Si_2O_6$ pyroxenes based on regular solution and cooperative disordering models. *Contributions in Mineral and Petrology* 69:377–344.

Hsieh K.-C., Vlacxh K. C., and Chang Y. A. 1987. The Fe-Ni-S system, I. A thermodynamic analysis of the phase equilibria and calculation of the phase diagram from 1173 to 1623 K. *High Temperature Science* 23:17–38.

Jarosewich E. 1990. Chemical analyses of meteorites: A compilation of stony and iron meteorite analyses. *Meteoritics* 25:323–337.

Joliff B. L., Haskin L. A., Colson R. O., and Wadwha M. 1993. Partitioning in REE-saturating minerals: Theory, experiment, and modelling of whitlockite, apatite, and evolution of lunar residual magmas. *Geochimica et Cosmochimica Acta* 57:4069–4094.

Johnson D. M., Hooper P. R., and Conrey R. M. 1999. XRF analysis of rocks and minerals for major and trace elements on a single low dilution Li-tetraborate fused bead. *Advances in X-ray Analysis* 41:843–867.

Jones J. H. 1995. Experimental trace element partitioning. In *Rock physics and phase relations—A handbook of physical constants*, Washington, D. C.: American Geophysical Union. pp. 73–104.

Jurewicz A. J. G., Mittlefehldt D. W., and Jones J. H. 1995. Experimental partial melting of the St. Severin (LL) and Lost City (H) chondrites. *Geochimica et Cosmochimica Acta* 59:391–408.

Kagi H., Takahshi K., Shimuzu H., Kitajima F., and Masuda A. 1991. In situ micro Raman studies on graphitic carbon in some Antarctic ureilites. *Proceedings of the NIPR symposium on Antarctic meteorites* 4:371–383.

Kagi H., Takahashi K., and Masuda A. 1994. Raman frequencies of graphitic carbon in Antarctic ureilites. *Proceedings of the NIPR symposium on Antarctic meteorites* 7:252–261.

Kenkman T., Hornemann U., and Stöffler D. 2002. Transformation of graphite to diamond in shock experiments: A Raman study (abstract #1052). 31st Lunar and Planetary Science Conference. CD-ROM.

Koblitz J. 2003. MetBase—Meteorite data retrieval software. MetBase version 6.0 for Windows. CD-ROM.

Komarek K. L. 1963. Direct reduction of iron ores containing phosphorus. *Transactions of the Metallurgical Society of AIME* 227:136–145.

Kong P. and Ebihara M. 1996. Metal phases of L chondrites: Their formation and evolution in the nebula and in the parent body. *Geochimica et Cosmochimica Acta* 60:2667–2680.

Kong P., Ebihara M., Nakahara H., and Endo K. 1995. Chemical characteristics of metal phases of the Richardton H5 chondrite. *Earth and Planetary Science Letters* 136:407–419.

Knack C., Cornelius S., and Hooper P. 1994. Trace element analyses of rocks and minerals by ICPMS. Department of Geology, Washington State University. URL: http://www.wsu.edu/%7Egeology/Pages/Services/ICP.html. Last accessed May 1, 2004.

Kring D. A., Hill D. H., and Gleason J. D. 1999a. Portales Valley meteorite: The brecciated and metal-veined floor of a >20 km diameter crater on an H chondrite asteroid (abstract #1618). 30th Lunar and Planetary Science Conference. CD-ROM.

Kring D. A., Hill D. H., Gleason J. D., Britt D. T., Consolmagno G. J., Farmer M., Wilson S., and Haag R. 1999b. Portales Valley: A meteoritic sample of the brecciated and metal-veined floor of an impact crater on an H chondrite asteroid. *Meteoritics & Planetary Science* 34:663–669.

Kubaschewski O. 1982. Iron-Binary phase diagrams. Berlin: Springer-Verlag. 185 pp.

Lapke C., Schmitt R. T., Kenkmann T., and Stöffler D. 2000. Raman microspectrometry of shocked graphite and impact diamonds from the Ries crater, Germany (abstract #1040). 31st Lunar and Planetary Science Conference. CD-ROM.

Langmuir C. H. 1989. Geochemical consequences of in situ crystallization. *Nature* 340:199–205.

Lindsley D. H. 1983. Pyroxene thermometry. *American Mineralogist* 68:477–493.

Lindsley D. H. and Anderson D. J. 1983. A two-pyroxene thermometer. Proceedings, 13th Lunar and Planetary Science Conference. *Journal of Geophysical Research* 88:A887–A906.

Liu M. and Fleet M. E. 2001. Partitioning of siderophile elements (W, Mo, As, Ag, Ge, Ga, and Sn) and Si in the Fe-S system and their fractionation in iron meteorites. *Geochimica et Cosmochimica Acta* 65:671–682.

Massalski T. B, Murray J. L., Bennett L. H., and Baker H. 1986. Fe-C phase diagram. In *Binary alloy phase diagrams*, vol. 1. Metals Park, Ohio: American Society for Metals. pp. 562–566.

McCoy T. J., Keil K., Clayton R. N., Mayeda T. K., Bogard D. D., Garrison D. H., Huss G. R., Hutcheon I. D., and Wieler R. 1996. A petrologic, chemical, and isotopic study of Monument Draw and comparison with other acapulcoites: Evidence for formation by incipient partial melting. *Geochimica et Cosmochimica Acta* 60:2681–2708.

McCoy T. J., Ehlmann A. J., Benedix G. K., Keil K., and Wasson J. T. 1996. The Leuders, Texas, IAB iron meteorite with silicate inclusions. *Meteoritics & Planetary Science* 31:419–422.

McKay G. A. 1986. Crystal/liquid partitioning of REE in basaltic systems: Extreme fractionation of REE in olivine. *Geochimica et Cosmochimica Acta* 50:69–79.

McKay G., Wagstaff J. and Yang S.-R. 1986. Clinopyroxene REE

distribution coefficients for shergottites: The REE content of the Shergotty melt. *Geochimica et Cosmochimica Acta* 50:927–937.
McSween H. Y., Jr. and Patchen A. D. 1989. Pyroxene thermobarometry in LL group chondrites and implications for parent body metamorphism. *Meteoritics* 24:219–226.
McSween H. Y., Jr. and Labotka T. C. 1993. Oxidation during metamorphism of the ordinary chondrites. *Geochimica et Cosmochimica Acta* 57:1105–1114.
McSween H. Y., Jr., Taylor L. A., and Lipschutz M. E. 1978. Metamorphic effects in experimentally heated Krymka (L3) chondrite. 9th Lunar and Planetary Science Conference. pp. 1437–1447.
Mittlefehldt D. W. 2002. Geochemistry of the ungrouped carbonaceous chondrite Tagish Lake, the anomalous CM chondrite Bells, and comparison with CI and CM chondrites. *Meteoritics & Planetary Science* 37:703–712.
Mittlefehldt D. W. and Lindstrom M. M. 1993. Geochemistry and petrology of a suite of ten Yamato HED meteorites. Proceedings, 17th Symposium on Antarctic Meteorites. pp. 268–292.
Miyamoto M. 1998. Micro Raman spectroscopy of diamonds in the Canyon Diablo iron meteorite: Implications for the shock origin. *Antarctic Meteorite Research* 11:171–177.
Moren A. E. and Goldstein J. I. 1979. Cooling rates of Group IVA iron meteorites determined from a ternary Fe-Ni-P model. *Earth and Planetary Science Letters* 43:182–196.
Murrell M. T. and Burnett D. S. 1983. The behavior of actinides, phosphorus, and rare earth elements during chondrite metamorphism. *Geochimica et Cosmochimica Acta* 47:1999–2014.
Olsen E. and Fuchs L. H. 1967. The state of oxidation of some iron meteorites. *Icarus* 6:242–253.
Papanastassiou D. A., Chen J. H., and Wasserburg G. J. 2001. Chronology and composition puzzles in Portales Valley (abstract #1476). 32nd Lunar and Planetary Science Conference. CD-ROM.
Papanastassiou D. A., Chen J. H., and Wasserburg G. J. 2002. What whole rock samples of Portales Valley can and cannot tell us (abstract #1826). 33rd Lunar and Planetary Science Conference. CD-ROM.
Pinault L. J., Scott E. R. D., Bogard D. D., and Keil K. 1999. Extraordinary properties of the metal-veined, H6 Portales Valley chondrite: Evidence for internal heating versus shock-melting origins (abstract #2048). 30th Lunar and Planetary Science Conference. CD-ROM.
Rambaldi E. R. 1977. Trace element content of metals from H and LL group chondrites. *Earth and Planetary Science Letters* 36:347–358.
Reisener R. J. and Goldstein J. I. 2003. Ordinary chondrite metallography: Part 2. Formation of zoned and unzoned metal particles in relatively unshocked H, L, and LL chondrites. *Meteoritics & Planetary Science* 38:1679–1696.
Rollinson H. 1993. Using geochemical data: Evaluation, presentation, interpretation. New York: Wiley & Sons. 352 p.
Rubin A. E. 1985. Impact melt products of chondritic material. *Reviews of Geophysics* 23:277–300.
Rubin A. E. 1990. Kamacite and olivine in ordinary chondrites: Intergroup and intragroup relationships. *Geochimica et Cosmochimica Acta* 54:1217–1232.
Rubin A. E. 1992. A shock-metamorphic model for silicate darkening and compositionally variable plagioclase in CK and ordinary chondrites. *Geochimica et Cosmochimica Acta* 56: 1705–1714.
Rubin A. E. 1993. Metallic copper in ordinary chondrites. *Meteoritics* 29:93–98.
Rubin A. E. 2003. Chromite-plagioclase assemblages as a new shock indicator; Implications for the shock and thermal histories of ordinary chondrites. *Geochimica et Cosmochimica Acta* 67: 2695–2709.
Rubin A. E. 2004. Postshock annealing and postannealing shock in equilibrated ordinary chondrites: Implications for the thermal and shock histories of chondritic asteroids. *Geochimica et Cosmochimica Acta* 68:673–689.
Rubin A. E. and Ulff-Møller F. 1999. The Portales Valley meteorite breccia: Evidence for impact-induced metamorphism of an ordinary chondrite (abstract #1125). 30th Lunar and Planetary Science Conference. CD-ROM.
Rubin A. E., Ulff-Møller F., Wasson J. T., and Carlson W. D. 2001. The Portales Valley meteorite breccia: Evidence for impact-induced melting and metamorphism of an ordinary chondrite. *Geochimica et Cosmochimica Acta*:66:323–342.
Rushmer T., Gaetani G., and Jones J. H. 2000a. Chondrites under stress: What can they tell us about core formation processes? (abstract #1673). 31st Lunar and Planetary Science Conference. CD-ROM.
Rushmer T., Minarik W. G., and Taylor G. J. 2000b. Physical processes of core formation. In *Origin of the Earth and Moon*, edited by Canup R. M. and Righter K. Tucson, Arizona: The University of Arizona Press. pp. 227–243.
Rushmer T., Humayan M., and Campbell A. J. 2004. Siderophile element abundances in Fe-S-Ni-O melts segregated from partially molten ordinary chondrite under dynamic conditions (abstract #1850). 35th Lunar and Planetary Science Conference. CD-ROM.
Ruzicka A., Snyder G. A., Prinz M., and Taylor L. A. 1999a. Portales Valley: A new metal-phosphate-rich meteorite with affinities to Netschaevo and H group chondrites (abstract #1645). 30th Lunar and Planetary Science Conference. CD-ROM.
Ruzicka A., Bennett M. E., III, Patchen A. D., Snyder G. A., and Taylor L. A. 1999b. Widmannstätten texture in the Portales Valley meteorite: Slow (but not unusually slow) cooling at low temperatures (abstract #1616). 30th Lunar and Planetary Science Conference. CD-ROM.
Ruzicka A., Killgore M., Boesenberg J., and Prinz M. 2000a. Portales Valley: Not just another "ordinary" chondrite (abstract). *Meteoritics & Planetary Science* 35:A139–A140.
Ruzicka A., McHone J. F., and Killgore M. 2000b. Portales Valley: Discovery of a large graphite nodule. *Meteoritics & Planetary Science* 35:A140.
Ruzicka A. and Killgore M. 2002. Trace element abundances in the Portales Valley meteorite: Evidence for geochemical fractionations (abstract #1918). 33rd Lunar and Planetary Science Conference. CD-ROM.
Scott E. R. D. and Pinault L. J. 1999. Partial melting and incipient segregation of troilite and metal in winonaites, acapulcoites, IAB and IIE irons, and fine-grained H6 chondrites (abstract #1507). 30th Lunar and Planetary Science Conference. CD-ROM.
Schwandt C. S. and McKay G. A. 1996. REE partition coefficients from synthetic diogenite-like enstatite and the implications of petrogenetic modelling. Proceedings, Workshop on the Evolution of Igneous Asteroids. pp. 25–27.
Sepp B., Bischoff A., and Bosbach D. 2001. Low-temperature phase decomposition in iron-nickel metal of the Portales Valley meteorite. *Meteoritics & Planetary Science* 36:587–595.
Stöffler D., Keil K., and Scott E.R.D. (1991) Shock metamorphism of ordinary chondrites. *Geochimica et Cosmochimica Acta* 55: 3845–3867.
Takahashi E. 1983. Melting of a Tamato L3 chondrite (Y-74191) up to 30 Kbar. 8th Symposium on Antarctic Meteorites pp. 168–180.
Treiman A.H. (1996) The perils of partition: Difficulties in retrieving magma compositions from chemically equilibrated basaltic meteorites. *Geochimica et Cosmochimica Acta* 60:147–155.
Usselman T. M. 1975. Experimental approach to the state of the core:

Part I. The liquidus relations of the Fe-Ni-S system from 30 to 100 Kb. *American Journal of Science* 275:278–290.

Van de Bogert C. H., Schultz P. H., and Spray J. G. 2003. Impact-induced frictional melting in ordinary chondrites: A mechanism for deformation, darkening, and vein formation. *Meteoritics & Planetary Science* 38:1521–1531.

Wasson J. T. 1985. Meteorites—Their record of early solar system history. New York: W. H. Freeman and Company.

Wasson J. T. and Wang J. 1986. A nonmagmatic origin of group-IIE iron meteorites. *Geochimica et Cosmochimica Acta* 50:725–732.

Wasson J. T. and Kallemeyn G. W. 1988. Compositions of chondrites. *Philosophical Transactions of the Royal Society of London A* 325:535–544.

Watson E. B. and Green T. H. 1981. Apatite/liquid partition coefficients for the rare earth elements and strontium. *Earth and Planetary Science Letters* 56:405–421.

Weill D. F. and McKay G. A. 1975. The partitioning of Mg, Fe, Sr, Ce, Sm, Eu, and Yb in lunar igneous systems and a possible origin of KREEP by equilibrium partial melting. 6th Lunar Science Conference. pp. 1143–1158.

Williams R. J. 1971. Reaction constants in the system Fe-MgO-SiO_2-O_2 at 1 atm between 900° and 1300 °C: Experimental results. *American Journal of Science* 270:334–360.

Yugami K., Takeda H., Kojima H., and Miyamoto M. 1998. Modal mineral abundances and the differentiation trends in primitive achondrites. *Antarctic Meteorite Research* 11:49–70.